"CFD Analysis of Wind Turbine Blade at Various Angle of Attack and Different Reynold Number"

Major project-II

Submitted to Delhi Technological University in partial fulfilment of the requirement for the award of Degree of

Master of Technology

In

Renewable Energy Technology

SUBMITTED BY-

MD GULAM MUSTAFA

2K15/RET/08

UNDER SUPERVISION OF

MR. M. ZUNAID

ASSISTANT PROFESSOR

Department of Mechanical Engineering
Delhi Technological University
(Formerly DELHI COLLEGE OF ENGINEERING)
Bawana road, Delhi -110042

CERTIFICATE

DELHI TECHNOLOGICAL UNIVERSITY
(Formerly DELHI COLLEGE OF ENGINEERING)

Date:-__________

This is to certify that report entitled **“CFD Analysis of Wind Turbine Blade at Various Angle of Attack and Different Reynold Number” by MD GULAM MUSTAFA** in the requirement of the partial fulfilment for the award of Degree of **Master of Technology (M.Tech)** in **Renewable Energy Technology** at **Delhi Technological University**. This work was completed under my supervision and guidance. He has completed his work with utmost sincerity and diligence. The work embodied in this project has not been submitted for the award of any other degree to the best of my knowledge.

Mr. M. ZUNAID
(Asst. professor)
Delhi technological university
Delhi

DECLARATION

I declare that the work presented in this thesis titled "CFD analysis of Wind Turbine Blade at Various Angle of attack and different Reynold number", submitted to Department of Mechanical Engineering, is an authentic record of my own work carried out under the supervision of asst. prof. Mr. M. ZUNAID, Department of Mechanical Engineering, Delhi technological university, Delhi.

This report does not, to the best of my knowledge, contain part of my work which has been submitted for the award of any other degree either of this university or any other university without proper citation.

Date:

Place: DTU, Delhi Signature of candidate

ACKNOWLEDGEMENT

First, I would like to express my gratitude to God for giving me ideas and strengths to make my dreams true and accomplish this thesis.

To achieve success in any work, guidance plays an important role. It makes us put right amount of energy in the right direction and at right time to obtain the desired result. Express my sincere gratitude to my guide, **MR. M. ZUNAID**, Asst. Professor, Mechanical Engineering Department for giving valuable guidance during the course of this work, for his ever encouraging and timely moral support.

I am greatly thankful to **DR. R. S. MISHRA**, Professor and Head, Mechanical Engineering Department, Delhi Technological University, for his encouragement and inspiration for execution of the this work. I express my feelings of thanks to the entire faculty and staff, Department of Mechanical Engineering, Delhi Technological University, and Delhi for their help, inspiration and moral support, which went a long way in the successful completion of my report work.

MD GULAM MUSTAFA

(Roll No-2K15/RET/08)

ABSTRACT

The rapid expansion of the wind energy market necessitates the need for advanced computational modeling and understanding of wind turbine aerodynamics and wake interactions. The following thesis work looks to study turbulence closure methods widely used in computational fluid dynamics (CFD) and their applicability for modeling wind turbine aerodynamics. The first investigation is a parametric study of turbulence models and their performance on geometries of stationary in-line turbines and disks spaced at different intervals. A variety of Reynolds-averaged Navier-Stokes (RANS) closure schemes (Spalart-Allmaras, Standard k-ε, k-ε Realizable, k-ε RNG, Standard k-ω, k-ω SST) were studied as well as a large eddy simulation (LES) with a dynamic Smagorinsky-Lilly sub-grid scale (SGS) model. The simulations showed the grid refinement to be inadequate for LES studies.

The investigation uses only the k-ω SST RANS closure scheme to model wake development and resolution for both a single fully resolved rotating turbine as well as two in-line fully resolved rotating turbines. These simulations were successful in predicting wake development and resolution, as well as predicting velocity deficits experienced by the downstream turbine. Vorticity results also showed an accurate wake structure and helical tendencies.

The results of thesis clearly shows the variation of C_l and C_d with angle of attack. Thus for a particular Reynold number the optimum angle of attack came between 350 and 400. With the increase in the Reynold number C_l also increases, and wind turbine efficiency increases by 20%.

In contrast to the vast super-computer simulations found in literature, all simulations in this thesis work were calculated using two parallel processors. The accuracy was achieved through assumptions, which were designed to maintain the desired physics while simplifying the complexity of the problem to the capabilities of desktop computing. This research demonstrates the significance of model design and capabilities and accuracy achievable using desktop computing power. This has vast implications of accessibility into academia and the further development of the wind power industry.

CONTENTS

Page No.

LIST OF FIGURES

LIST OF TABLE

NOMENCLATURE

ABL	Atmospheric boundary layer
ADM	Actuator Disk Model
FEM	Finite Element Method
FSI	Fluid-Structure Interface
HAWT	Horizontal Axis Wind Turbine
VAWT	Vertical Axis Wind Turbine
NREL	National Renewable Energy Laboratory
SST	Shear Stress Transport
LLJ	Low level jet
RANS	Reynolds-Averaged Navier-Stokes
RNG	Renormalization Group
CFD	Computational Fluid Dynamics
BEM	Blade Element Method
k	Turbulent Kinetic energy (m^2s^2)
ε	Rate of dissipation of turbulent kinetic energy (W/kg)
ω	turbulence frequency
μ	Dynamic Viscosity(N-s/m^2)
σ	Stress (MPa)
ρ	Density (Kg/m^3
τ	Shear stress (MPA)
υ	Kinematic Viscosity (m^2/s)
λ	Tip speed ratio
ω	Specific dissipation rate
a	Axial induction factor
C_L	Lift coefficient
C_D	Drag coefficient
S	Strain rate
F	Wind speed probability
c	Weibull parameter
U	Wind velocity (m/s^2)
A	Swept area of rotor (m^2)

Re	Reynold number
u	Mean velocity (m/s^2)
T	Thrust (m)
P	Power (W)
P_{avail}	Available power (W)
T_{avail}	Thrust available (N)
u(t)	Fluctuation in wind velocity (m/s^2)
C_T	Thrust Coefficient
G_k	Kinetic energy production due to mean velocity
G_b	Kinetic energy production due to buoyant force
G_ω	Kinetic energy production due to velocity gradient
z_0	Roughness length
D_ω	Cross-diffusion
a_1	Closure coefficient
F_2	Second blending function

CHAPTER 1

INTRODUCTION

1.1 Motivation and objective

The fast depletion of energy resources from the earth is the main cause of concern for the human race. These are mainly non-renewable energy source like fossil fuel, which are also responsible for global changes in climate. The EIA estimates that 86% of energy requirement meant by burning of fossil fuel [40]. Formation of fossil fuel takes millions of year, but consumption of it is rapid. With such rate of depletion these fossil fuel are in near end of its time. Another evil associated with fossil fuel is emission of large amount of harmful gases in the atmosphere. By burning fossil, we deposit 10.85 tonne of carbon monoxide in atmosphere [40], which unbalance the atmosphere condition. Therefore, there is need of renewable energy source, which is clean and safe.

Renewable energy sources are the type of energy sources, which are plenty in quantity and derived from earth. Wind energy, solar energy, geo thermal and bio mass are different types of renewable energy sources. These resources are inexhaustible in nature. The known advantages of renewable energy sources are its clean nature, abundant in quantity and most importantly, it is eco-friendly unlike non-renewable energy sources. Now days more research is going on the enhancement of technology, which can efficiently convert the renewable energy sources into useful electrical energy sources. Though the literal conversion efficiency of renewable energy sources is lower than that of conventional energy source, the technology is developed and improvised on daily basis to improve its efficiency above 90%. On the other hand, conventional sources of energy are contributing towards pollution; it is depleting in quantity and exhaustible. Because of several disadvantages, renewable energy sources used as alternatives to it.

Wind turbine technology is consider one of the most promising areas of renewable energy sources. Most importantly, wind turbine operation does not emit any greenhouse gases. However, the manufacturing and installation of wind turbines are quite costly and produce pollutants.

The intent of this thesis is to:

1) A parametric study of CFD turbulence models to be used in wind turbine blade simulation;
2) Investigate the GE's 1.5xle turbine, which has airfoils S818, S825 and S826 for the root, body and tip, respectively.
3) Examine the variation of C_l and C_d at various Reynold number and angle of attack, and to obtain optimum angle of attack for Reynold number.

1.2 Brief History of Wind Turbine

The energy of the wind has been utilized since early recorded history all across the world. There are certain proofs that wind energy propelled boats along the river Nile around 5000 B.C. The Europeans got the idea of using wind power from the Persians who introduced it into the Roman Empire by 250 A.D. However, the first practical windmills were made in Afghanistan around 7th century of our era. Since then, technology has been improving so by the end of the 11th century people in the Middle East were using windmills extensively for food production. Returning merchants and crusaders carried this idea back to Europe where the Dutch refined the windmill and adapted it for draining lakes and marshes in the 1300's.

Professor James Blyth built one of the first larger windmills in Scotland in 1887 from Glasgow. Blyth's 10 m high, cloth-sailed wind turbine was installed in the garden of his holiday cottage and was used to charge accumulators that powered the lighting in the cottage electricity. The industrialization led to a gradual decline in the use of wind for such purposes.

In Denmark, wind power has played an important role since the first quarter of the 20th century. In 1956, a 24 m diameter wind turbine was installed at Gedser, where it ran until 1967. This was a three bladed, horizontal axis, upwind, stall regulated turbine similar to those used nowadays for commercial wind energy development.

The popularity of using wind energy has always fluctuated with the price of fossil fuels.

When fuel prices fell in the late 1940's, interest in wind generators decreased. However, when the price of oil went up in the 1970's the worldwide interest in wind turbine generators went up again. These first three parts in this chapter is derived from [42] and [43].

1.3 World Wide Energy Report 2010

How much installed wind power capacity does the earth have today? In this section some key elements from the World Wide Energy Report 2010, [44], prepared by The World Wind Energy Association (WWEA), will be presented. The WWEA is a non-profit organization, which works for a world energy system fully based on the various renewable energy technologies, with wind energy as one of the cornerstone. WWEA acts as a communication platform for all wind energy actors worldwide. The organization also advises national governments and international organizations on Reynolds 33 policies for wind energy implementation.

Key elements from their report from the 10th World Wind Energy Conference and Renewable Energy Exhibition in Cairo, Egypt from the 31st of October to the 2nd of November 2010:

- As of 2010 the world wide wind capacity reached 197 GW with a slight decrease in new capacity.
- China has become the world leader in installed wind energy, installing 18.9 GW, more than 50% of the world market.
- Of the total world capacity of 197 GW installed wind power, 37 GW was added in 2010, slightly less than in 2009.
- Wind power showed a growth rate of 23.6%, the lowest growth since 2004 and the second lowest the past decade. One of the likely causes of this was the aftermath of the global economic recession.
- All wind turbines installed by the end of 2010 worldwide can generate 430 Terrawatthours per annum, more than the total electricity demand of the United Kingdom, the sixth largest economy of the world and equalling 2.5% of the global electricity consumption.
- Many Western European countries stagnation in installation of wind turbines, whereas there is a strong growth in this area in Eastern European countries.
- Germany keeps its number one position in Europe with 27215 MW of installed effect, followed by Spain with 20676 MW.
- The highest shares of wind power was found in three European countries: Denmark (21%), Portugal (18%) and Spain (16%).

- Asia accounted for the largest share of new installations (54.6%) followed by Europe (27%).
- Latin America (1.2%) and Africa (0.4%) still played only a marginal role in new installations.
- WWEA sees a global capacity of 600’000 MW, 600 GW, as possible by the year 2015 and more than 1500 GW by the year 2020.

1.4. Size of wind turbine

The issue of what size of turbine produces energy at minimum cost has been debated for a long time. Spokespersons for large machines cite economics of scale and the increase in wind speed with height in their favour [41]. Opponents of this camp think about the “square-cube law”, whereby energy capture increases as the square of the diameter while rotor mass increases with the cube and thus is governing the costs. In reality, both arguments are correct, and there is a trade-off between economies of scale and a variant of the “square-cube law” which takes into account the wind shear effect. This trade-off can be examined with the help of simple cost modelling, but this will not be considered in this thesis. Further information on this subject can be found in Wind Energy Handbook, [41].

The European Wind Energy Association, EWEA, has the opinion that 20 MW wind turbines are technically feasible and could be the most cost efficient option for expanding Europe’s offshore wind energy capacity. This is according to the recently published results of “Upwind”, the largest EU-funded wind energy project ever, [47]. Today one can find offshore wind turbines up to 6 MW. Although there is a clear desire to build 20 MW turbines, one should rather do a stepwise scale-up in order to understand what is feasible with today’s technology and what needs to be improved in order to build a wind turbine of this magnitude.

A very problematic area even on turbines of today’s size is the large weight of the nacelle at the top of the turbine. For a 20 MW turbine this weight would be immense, so new technology will be needed to keep this weight at a reasonable level.

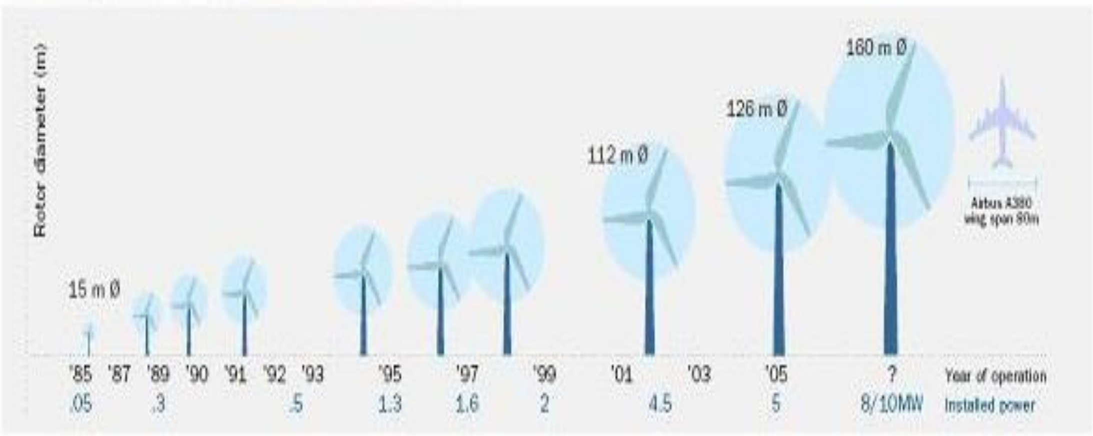

Figure 1.1 Size evolution of wind turbine [48]

1.5 Modern Wind Turbine

In the past, power generated from sources like coal, natural gas, nuclear fuel was considerably cheaper than wind power. However, with increases in fossil fuel costs and improvements in wind turbine technology, the playing field is starting to level.

1.5.1 Orientation

There are two orientations of wind turbines: horizontal axis wind turbines (HAWT) and vertical axis wind turbines (VAWT). There are advantages and disadvantages to each orientation. VAWTs use drag forces to rotate their blades and are frequently referred to as drag machines. The dominant advantage to a VAWT is that it can accept wind from any direction at any time. This means that it does not require any yaw system to align the turbine in the direction of the incident wind field. The blades are commonly straight without any taper along the long axis. This allows them to be manufactured at lower cost. Since they rotate about the vertical axis the drive train can be located near the ground, which reduces the maintenance costs. Although VAWTs can accept wind from any direction, they are less efficient than HAWTs. Another major problem with VAWTs is their scalability in terms of viability for commercial production. They also tend to see larger fatigue damage on the blades at the rotor as a result of cyclic aerodynamic stresses (McGowan, 2000).

In contrast, HAWTs use lift forces to rotate their blades and are frequently referred to as lift machines. HAWTs can be designed such that the turbine is either upstream or downstream from the supporting tower. In the downstream version, the turbine automatically aligns its self with the wind; this rotation is known as yaw. To assist with their free yawing capability, the rotor blades are coned slightly in the downwind direction. Downstream HAWTs are influenced by tower wind shadow. Since the supporting tower is upstream of the rotor, a wake is created by the tower. The main effect of this wake is uneven air loading on the blades, which causes an uneven angle of attack on the blades and leads to decreased efficiency. In addition, the uneven cyclic loading causes fatigue damage not only to the blades but to the tower and drive train as well. To a lesser extent the downwind orientation also causes increased noise output.

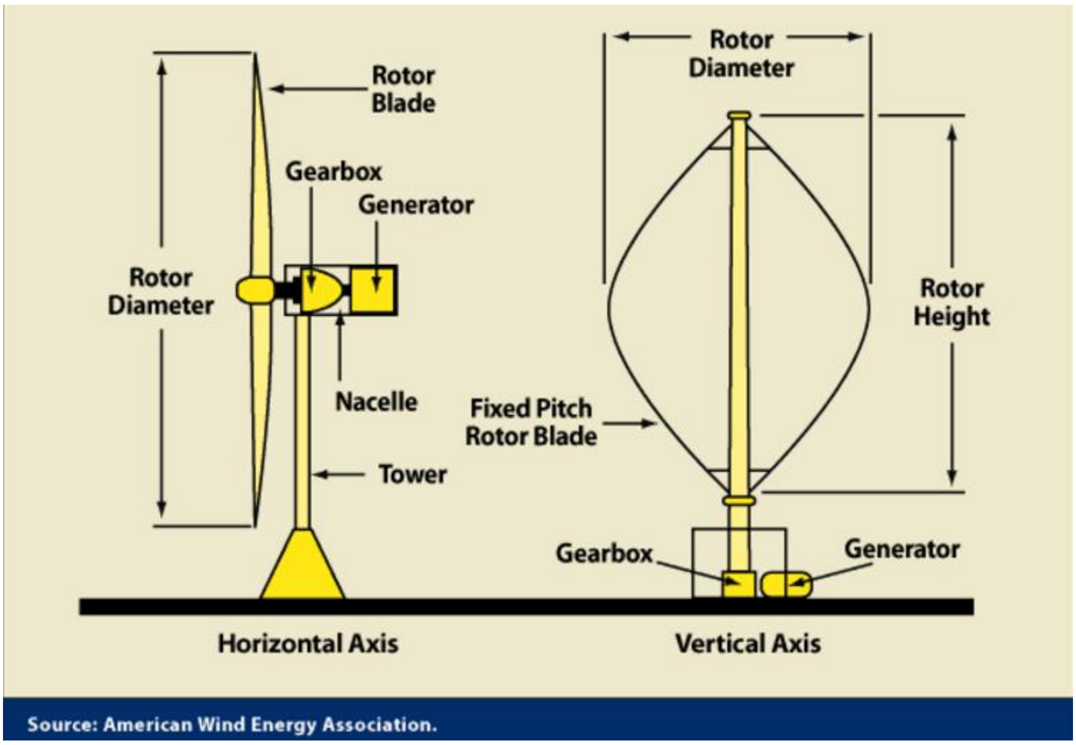

Source: American Wind Energy Association.

Figure 1.2. Type of wind turbine [40]

1.5.2 Rotational speed

There are two types of rotors: fixed speed rotors and variable speed rotors. The entire design of a fixed speed rotor is based on the requirements of the generation system and the gearbox. This type of design can experience decreased efficiency when wind speeds are not optimal. Fixed speed rotors make up the majority of wind turbines currently in use, however variable speed rotors are gaining in market share.

Variable speed rotor designs allow more wind energy to be captured. They also reduce the loading on the rotor and drive train components. Because variable speed rotors produce variable power output, power electronic converters are required for a turbine to be tied into the grid. Power electronic converters change the power output to the voltage and frequency required for transmission on the grid. They also allow a more flexible choice in generator.

1.5.3 Rotor characteristic

Rotor design and analysis is largely focused on maximizing the power coefficient as a function of tip-speed ratio. The tip-speed ratio is the ratio of the blade tip-speed to incoming wind speed. This ratio is also directly related to solidity, which reduces the cost of power generation. As a result, a longer blade produces a greater tip-speed ratio and a higher the rotational speed. A greater rotational speed lowers the torque on the drive train for a given power output. This increase in rotational speed, however, is noisier and increases the fouling of the blade (build-up of insects and dirt on the leading edge of the blade, which increases the frictional coefficient) (McGowan, 2000).

While typical rotors are designed with three blades, some rotors have only two. Rotors designed with three or more blades have a constant polar moment of inertia with respect to yawing. This allows for smooth yawing operations. Two rotor blade designs have a lower polar moment of inertia when the rotors are vertical and a higher polar moment of inertia when the rotors are horizontal. This oscillation causes cyclic loading and increased fatigue damage.

1.5.4 Aerodynamic power control

Because high winds can cause damage to wind turbines, they need to be designed with aerodynamic controls to maintain power. These controls include stall control, variable pitch control and yaw control. Stall control alters the wind’s angle of attack on the blades of the rotor. This is generally accomplished by the introduction of an induction generator. Stall control is commonly coupled with blades that are fastened rigidly to the hub. While maximum power generation is achieved at increased wind speeds, there is some power loss at lower wind speeds. The stall control method is not sufficient during extreme wind events, so an additional mechanical break is necessary to prevent damage.

Variable pitch control is accomplished by changing the angle of the blades along their long axis. This decreases the lift force available to turn the rotor and allows for more control than a stall control. Variable pitch control requires a more complicated hub assembly in order to have the desired mechanical control. As a variation on the full blade pitch control, there are some designs that have an option for partial span pitch control.

Yaw control achieves aerodynamic power control by turning the rotor away from the dominant wind direction. This method requires a very robust yaw control system able to operate with increased torques.

1.5.5 Rotor and blade characteristic

Recently the National Renewable Energy Laboratory (NREL) designed a series of ten blades to address issues surrounding wind turbine aerodynamics. This new series of blades are insensitive to blade surface roughness, which means that fouling is not a consideration. The series was also designed to address the needs of stall, variable pitch, and variable rotation control. Contemporaneous with the production of the NREL blades, Risø National Laboratory in Europe designed a series of six blades. This series is also insensitive to surface roughness. They were able to achieve lift coefficients of 1.5 and high lift-to-drag ratios for high angles of attack. Another feature of the Riso blades was the implementation of trailing edge stall capabilities.

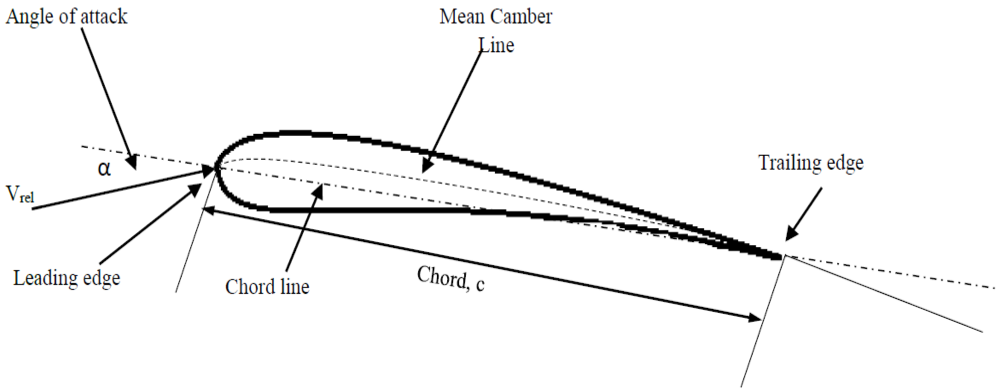

Figure 1.3 Airfoil Profile Nomenclature

1.6 Overview of Horizontal Axis Wind Turbine

The most popular wind turbine today and the design, which has been taken in by the companies producing windmills, is the horizontal one. This is mainly due to a higher efficiency and a better overall economic profile than what the vertical axis wind turbine.

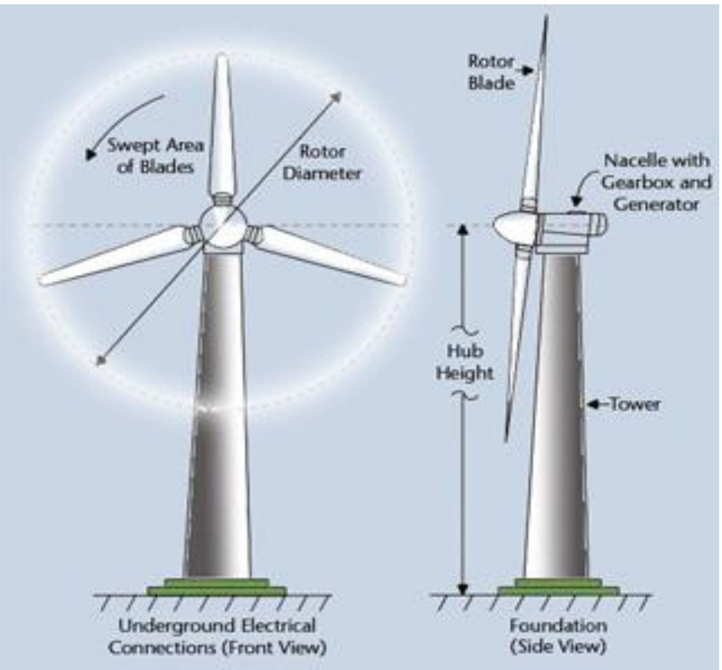

Figure 1.4 Wind Turbine With basic elements [48]

1.6.1 Power and location

Power available is in wind is given by

$$P = \frac{1}{2}\rho A U^3 \qquad 1.1$$

Where ρ is the density of air (1.225 kg/m3), A is the rotor swept area and U is the wind speed.

Before choosing a location to set up a windmill the wind conditions in that specific area needs to be investigated. During this process the normal procedures is to use the Weibull distribution and wind roses. A wind rose is a diagram showing the direction and speed of the wind over some period of time. Due to its similarities with a flower it gets its name, wind rose. The Weibull distribution is a two-parameter function used to fit the wind speed frequency distribution [27]. The Weibull function provides a convenient representation of the wind speed data for wind energy calculation purposes. In wind analysis it is used to represent the wind speed probability density function, PDF, commonly referred to as the wind speed distribution. The relation between the probability density function and the cumulative density function is

$$CDF(U) = P(U \leq u) = \int_{0,-\infty}^{u} PDF(u) \qquad 1.2$$

The Weibull distribution function as a cumulative density function [28] is given by

$$F(U) = 1 - e^{-(\frac{U}{c})^k} \qquad 1.3$$

F is the wind speed probability, k is the shape factor, c is the Weibull parameter or scale factor and U is the wind velocity. The shape factor is related to the width of the distribution. A low shape factor indicates that the deviation from the average wind occurs more often than if one had a high shape factor. In an area with a high shape factor, the observed wind lays closer to the average wind speed and the wind conditions are therefore more stabile. A low shape factor can be a sign of areas that are more prone to storms or that have long periods of little wind. A high shape factor will produce a narrow and high graph. The Weibull parameter, c, is the weighted average speed. A large c generally means stronger wind.

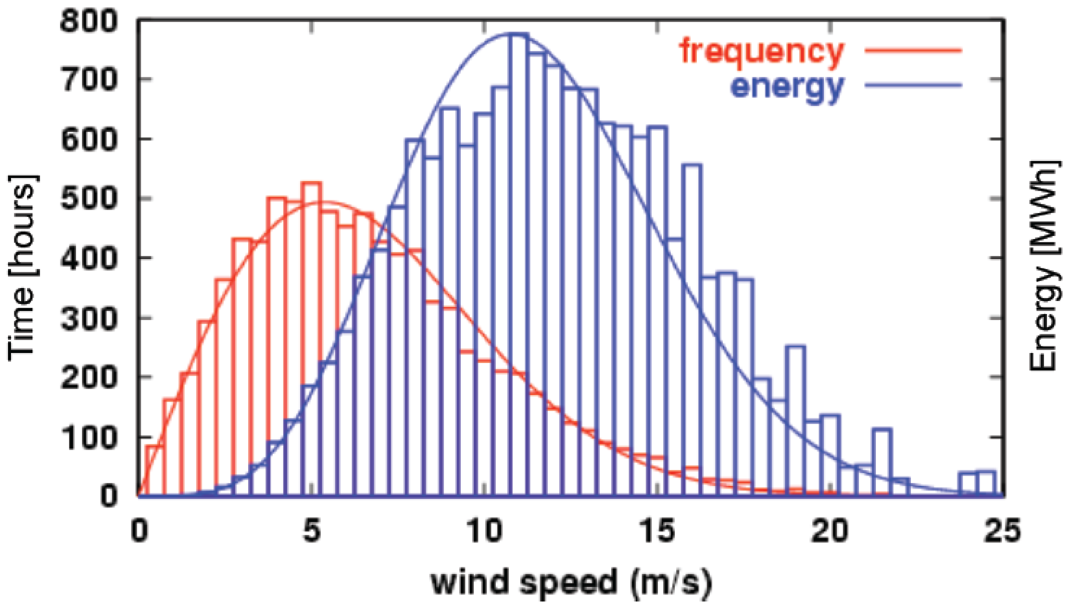

Figure 1.5 Weibull distribution in red and energy in wind in blue [51].

The energy varies with wind velocity to the power of 3, and the maximum energy in the wind weighted with how often a certain wind speed occur gives a maximum at a higher wind speed than the winds that are most often occurring. Because of this, windmills are designed to achieve maximum torque at a higher wind speed than the average wind speed at a given location.

1.6.2 Power coefficient

$$P = \frac{1}{2}\rho A U^3 C_p \qquad 1.4$$

Where C_p is power coefficient, which is limit to power extracted. According to Betz Theorem [6] the limit is 0.5926. This limit based on Momentum theory and uses global control volume analysis to provide information on how much energy can be captured from the wind. However, because there always are losses in a wind turbine operation such as in the gearbox, generators, electric wiring and aerodynamic losses this limit remains only theoretical. Some examples of aerodynamic losses are

- Contamination of bugs; when the blade contaminates with bugs and insects it will cause the maximum lift to fall.
- At times, the wind turbine might operate in the wake of another turbine; this will cause the turbine to lose power production.
- The larger the turbine, the more the incoming wind deviates in speed, direction and turbulence intensity along the blade.
- Drag, stall and 3D effects like tip losses will obstruct the quest in reaching Betz limit.

The power coefficient of a rotor varies with the tip speed ratio,

$$\lambda = \frac{\omega R}{U} \qquad 1.5$$

The tip speed ratio says something about the relationship between incoming velocity, U, the length of the blade, R, and the rotational speed of the rotor, ω. The Cp is only a maximum for a unique tip speed ratio.

In equation (1.5), the only parameter one has control over is the rotational speed. As the wind varies, different control systems come into action in order to change the rotational speed in such a way that a maximum power coefficient is maintained.

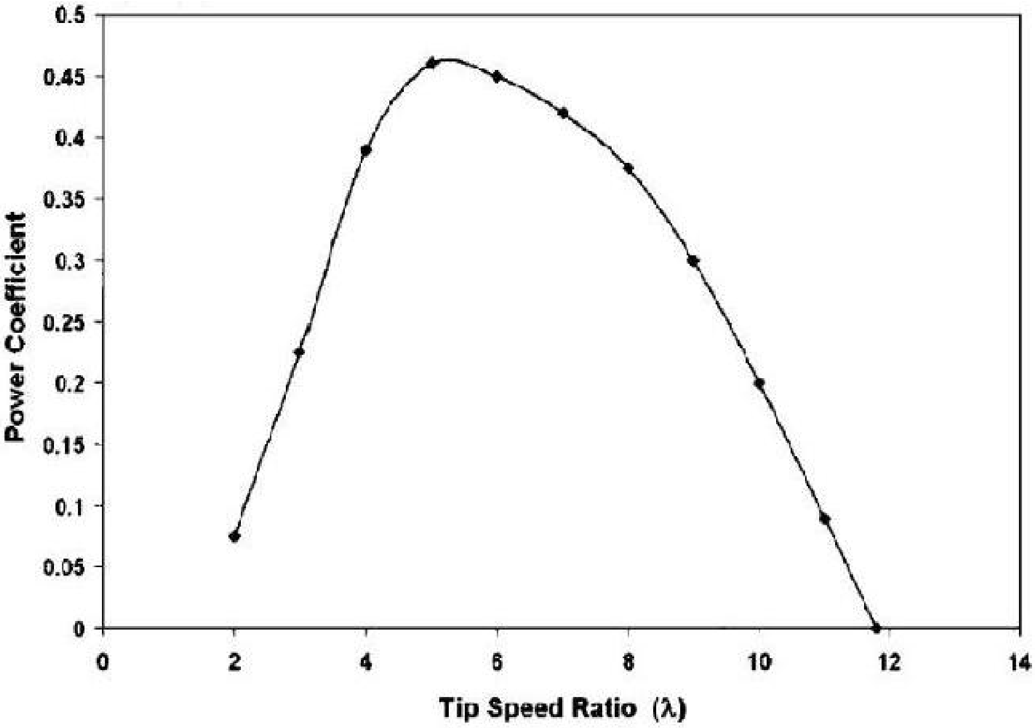

Figure 1.6 Power coefficient vs tip speed ratio [29].

1.6 Thesis Layout

The technical portion of this thesis is divided into four chapters. Chapter 2 presents a literature review of relevant scholarly publications. This information is present as both conceptual descriptions as well as case study discussions. The research provided in this Chapter builds a strong foundation for understanding current methods for the study of wind turbines.

Chapter 3 investigates the applicability of commonly used commercial CFD turbulence closure methods to the problem of wind turbine wake modelling. This was accomplished through both a literature review of turbulence closure methods, as well as a parametric study of turbulence models using CFD simulations of flow over stationary turbines and stationary disks. The performance of the turbulence models was assessed and an appropriate model was chosen for further study.

Chapter 4 builds upon the parametric study by continuing with the appropriate turbulence closure method, and using it in simulations of rotating turbines. These rotating simulations give insight into the wake structure, formation, interaction with downstream turbines, and resolution. Chapter 4 continues with a grid independence study, comparing the C_l and C_d at different angle of attack for a particular Reynold number. Load distributions on the turbine blades are then one-way coupled to a separate collaborative structural study.

Chapter 5 summarizes and concludes the main results and findings of this thesis work. Future direction and areas of study are also discussed.

CHAPTER 2

LITERATRE REVIEW

It is the intent of the literature review to encompass the subject matter critical for understanding and comprehensively modelling wind turbine wake interactions. The literature review will cover the blade element momentum theory, elementary wind models, power curves, and previous CFD (Computational fluid dynamic) studies.

2.1 Blade Element Momentum Theory

The Blade Element Momentum (BEM) model is the most fundamental method for wind turbine analysis. Originally developed by Glauert in 1935 for analysis of airplane propellers, it is a one-dimensional approach that models thrust as a function of wind speed. The principal function of the BEM model is to determine the conditions for maximum energy conversion (Leishman, 2006). There are several assumptions that are necessary to make the BEM method valid. They include a frictionless, incompressible, steady flow with no rotational velocity component. The rotor modelled as a permeable disk, and there are no external forces that act on the fluid upstream or downstream of the rotor. Drag is obtained by modelling a pressure drop over the rotor (Hansen, et al. [19]. Figure 2.1 shows the assumed conditions of the standard BEM model.

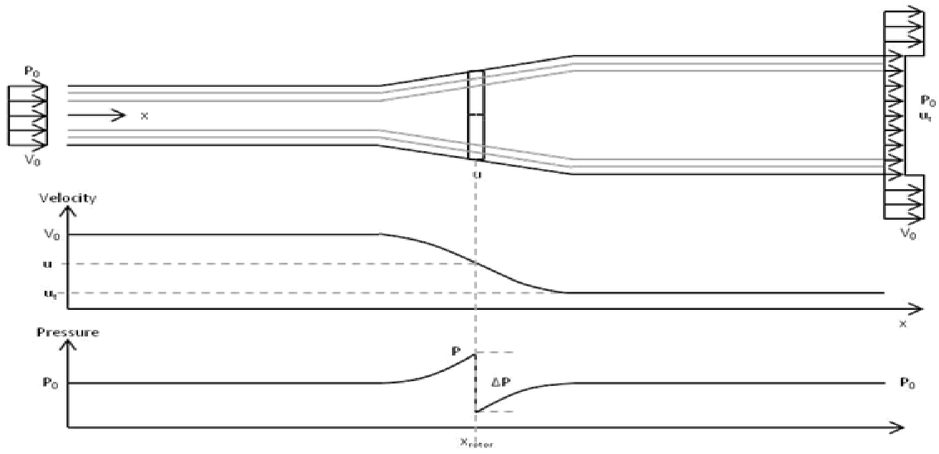

Figure 2.1 Assumed streamlines over the rotor, velocity and pressure up and downstream of the rotor [19].

With these assumptions for an ideal rotor, the relationships between the velocities V_0, u, and u_t (where V_0 is the upstream velocity, u is the velocity at the rotor, and u_t is the velocity in the wake downstream of the rotor), the thrust, and power, can be derived. The thrust force is, $T = \Delta p A$ 2.1

Where A is the swept area of the rotor.

Based on these assumptions, it is easy to apply Bernoulli's equation twice for the flow upstream to the rotor and from the rotor to the downstream flow. This gives:

$$p_0 + \frac{\rho V_0^2}{2} = \rho \frac{\rho u^2}{2} \tag{2.2}$$

$$(p - \Delta p) + \frac{\rho u^2}{2} = p_0 + \frac{\rho u_1^2}{2} \tag{2.3}$$

Combining Equations 2.2 and 2.3, Δp can be obtained as:

$$\Delta p = \frac{\rho}{2}(V_0^2 - u_1^2) \tag{2.4}$$

With this relationship known, the axial momentum equation can be examined, by viewing the control volume, Figure 2.2.

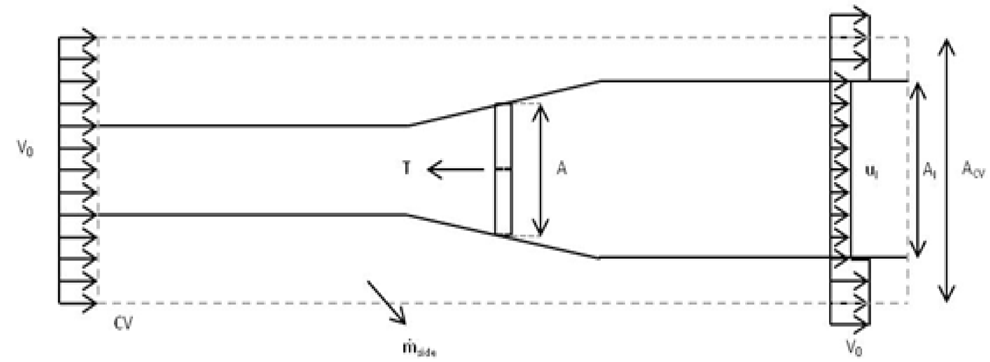

Figure 2.2 Cylindrical control volume around a wind turbine [19].

Since the flow is assumed to be steady, the first term in the momentum equation is zero. F_{ext} represents the pressure on both ends. Since the pressure is equal and it acts on the same area, F_{ext} is zero. F_{press} is the axial component of the pressure acting on the lateral boundary of the control volume. There is no axial pressure on the lateral boundary. $\underset{dA}{\rightarrow}$ is a vector normal to the control surface with a length equivalent to the infinitesimal area of the element.

Since the system is assumed to be frictionless it follows that there is no loss of internal energy. This yields the equation for the potential power captured as,

$$P = \dot{m}(\frac{1}{2}V_0^2 + \frac{p_0}{\rho} - \frac{1}{2}u_1^2 - \frac{p_0}{\rho}) \qquad 2.5$$

It is at this point that it is appropriate to introduce the simplification of an induction factor, $a = 1 - \frac{u}{V_0}$.

The power equation can be written in terms of a as,

$$P = 2\rho A V_0^3 a(1-a)^2 \qquad 2.6$$

The thrust equation can also be written in terms of a as,

$$T = 2\rho A V_0^2 a(1-a) \qquad 2.7$$

The power and thrust can both be non-dimensionalized in terms of a power coefficient and a thrust coefficient. The power coefficient is the ratio of power to the amount of power available, P_{avail}, over the swept cross-sectional area. This reduces as,

$$C_p = \frac{P}{P_{avail}}$$

$$C_p = 4a(1-a)^2 \qquad 2.8$$

Likewise the thrust coefficient is the ratio of thrust to the amount of thrust available, T_{avail} , over the swept cross-sectional area. This reduces as,

$$C_T = \frac{T}{T_{avail}},$$

$$C_T = 4a(1-a) \qquad 2.9$$

The BEM method is very sensitive to the value of a. Since the thrust and power cannot exceed their available amount it can be inferred that C_T and C_P cannot exceed one. This is not a problem for the coefficient of thrust, as its value will be less than one for any value of a. However, the coefficient of power requires a not to exceed 1.42. This is an illogical value since the velocity over the turbine cannot be negative or greater than the upstream velocity. This requirement limits to greater than zero and less than one. The controlling limit comes from the assumption of constant streamlines. When a exceeds 0.4, the momentum theory is no longer valid, and the free shear layer in the wake becomes unstable and large eddies form in the wake resulting in negative velocities. This is known as a turbulent wake state. A turbulent wake state invalidates many of the assumptions on which the BEM method is based. Figure 2.3 shows the relationship between a and C_T and C_P.

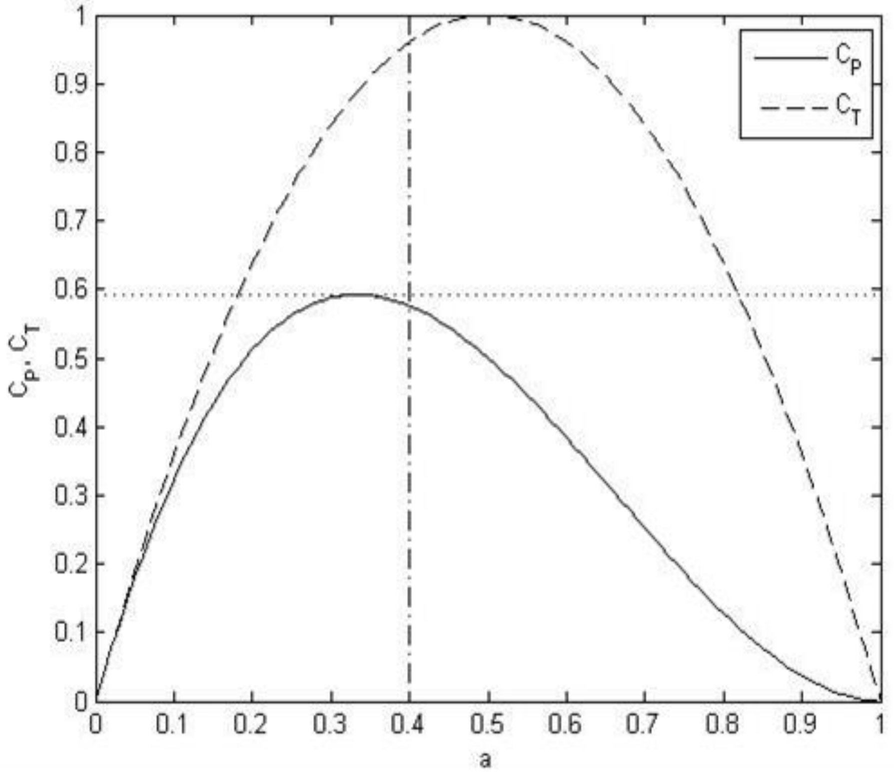

Figure 2.3 Trends of C_T and C_P with maximum a and C_P shown for an ideal HAWT [19].

It can be seen that the maximum C_P occurs at a equal to 1/3. The value of C_P is 0.59 and C_T is 0.89 [23]. The theoretical maximum power output is known as the Betz limit [19]. This occurs at higher upstream wind speeds and thus higher values of a.

There are many weaknesses with the BEM method. It does not account for values of a larger than 0.4 because of the turbulent wake state. This problem is also present at smaller values of a, because of the pressure term from the rotation of the wake being discarded.

Madsen et al. [24] addressed this problem with a numerical study of an actuator disk. They were able to pinpoint the physics that were causing these misrepresentations in the BEM (blade element method) method and suggested modifications that closely matched their results. The first problem was that the rotation of the wake was causing a slight resistance toward the hub of the rotor. To address this issue, they suggested adding an integral adjustment over the radius to the induced velocity (V_0-u). The second problem was that the centrifugal forces in the rotating wake were causing a decreased induction toward the tip of the rotor. In response, Madsen et al. similarly suggested subtracting an integral adjustment over the radius from the induced velocity. With both of these integral adjustments to the induced velocity, their study found very similar results between the numerical analysis of an actuator disk and the modified BEM method.

Modifications to the BEM method now allow for rotational, induction factor, and tip loss corrections (Hansen et al. [19]). These modifications make the BEM method an integration over the span of a blade. This is implemented in some codes, the most popular of which is the NREL AeroDyn code incorporated in FAST, the structural mechanics code published by NREL (Jonkman et al. [21]. The benefits of using BEM include rapid calculations, consideration of rotational wakes, increased induction factors, and tip loss corrections. BEM is also reasonably accurate for the model of wind speeds around the rated wind speed.

L. Wang et al. [54] developed a FSI model; model was coupled with CFD and FEA. The increasing size and flexibility of large wind turbine blades introduces considerable aeroelastic effects, which are caused by FSI. The maximum blade-tip flapwise deflection (1.785 m) was observed at 12 m/s wind speed case, which is lower than the tower clearance (3.3 m).

2.2 Elementary Wind Models

Many factors affect power generation in wind turbines. Some of the more considerable ones are the wind speed, the equivalent density altitude, wind gusts, and the tower height. The tower height is important because wind velocity gradients can change substantially in the ABL (Atmospheric boundary layer). This velocity gradient is highly dependent on surface terrain conditions, much like pipe flow and open channel flow. However, in ABLs, stratification plays a significant role in velocity gradients and boundary layer formation. The reduced velocity at lower elevations also reduces the overall mass flow through the turbine, reducing the total power output and increasing the fatigue over the life of the turbine. These factors are very important for wind farm design and placement. This study includes the modelling of the boundary layer velocity gradients. Since it is prohibitive to study wind patterns at elevations as high as those of implemented turbines, measurements are generally performed at an elevation of ten meters. This data then needs to be extrapolated to the elevation of the potential wind turbines. The most elementary models, as described by Leishman et al. [23], for predicting the neutral boundary layer are the power law and the logarithmic law. It should be noted that these methods only produce reasonable predictions for perfectly neutral ABL flow.

The power law states:

$$V_\infty(h) = V_\infty(h_{ref})\frac{ln\frac{h}{z_0}}{ln\frac{h_{ref}}{z_0}} \qquad 2.10$$

Where z_0, is the roughness length. Both the power law and logarithmic laws are only valid for flat terrain. C Aniket et al. [58] validate a solver including a transition model for wind turbine flows. An optimum tip speed ratio exists for aerodynamic performance at a given wind speed When topographical features are considered, a full CFD model is necessary. Typical values for z_0 and m shown in below Table 2.1

Table 2.1 Typical values of z_0 and m [23].

Type of terrain	z_0(m)	m
Open country	0.02	0.12
Rural with few trees	0.05	0.16
Rural with trees and town	0.30	0.928
Open Water	0.001	0.01

Typical logarithmic velocity profiles shown in Figure 2.4. For this example, a velocity of 13.4 meters per second was used. The wind turbine pictured modelled with 100-meter diameter blades and a hub height equal to 1.5 times the diameter (D) of the blades.

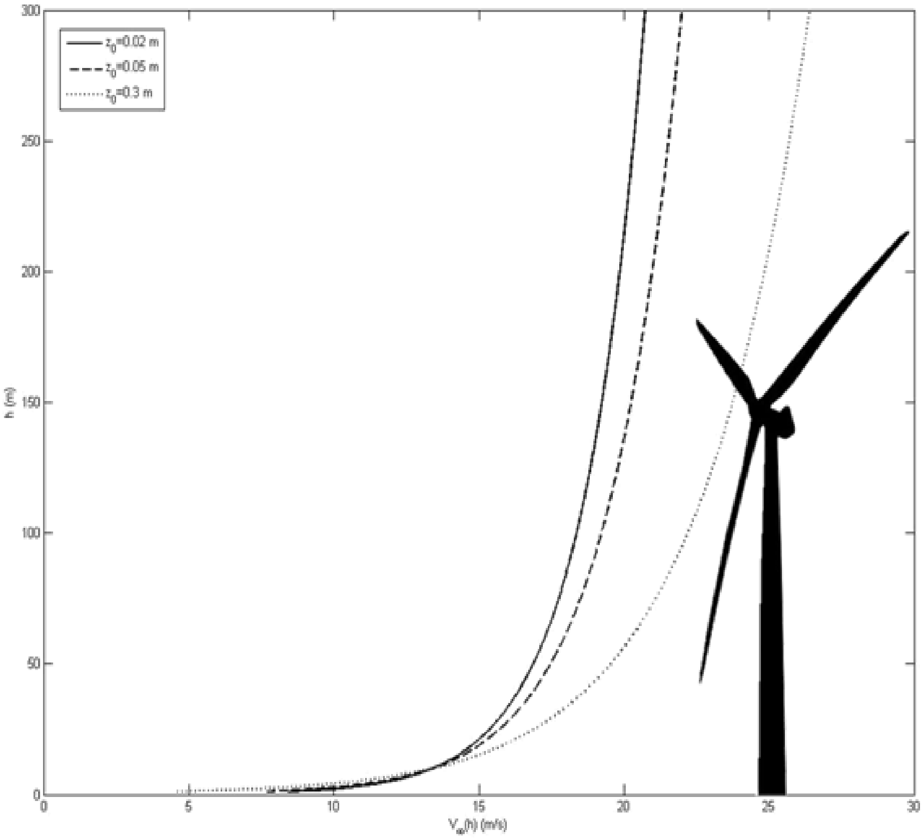

Figure 2.4 Logarithmic boundary layer velocity profiles for varying roughness coefficient, with a reference wind speed of 13.4 m/s. [23]

Since the wind is rarely constant, stochastic variations as a result of turbulence must be considered since they affect the power output of the turbine. The velocity as a function of time can be represented by $V_\infty(t)$,

$$V_\infty(t) = \bar{u} + u(t) \qquad 2.11$$

Where u is the mean wind velocity and $u(t)$represents the fluctuation in wind velocity at time . This information is more commonly used as part of a turbulence intensity factor,

$$I_u = \frac{1}{\bar{U}}\left[\int_0^t u(t)^2 dt\right]^2 \qquad 2.12$$

Where U is the total time was measured, generally ten minutes. In practice, I_u ranges between 0.1 U and 0.2 U , although it can be higher if the upstream terrain is rough. For design purposes, it is important to note that as the height of the tower increases the turbulence intensity decreases. In addition, the turbulence intensity factor is generally higher for lower wind speeds.

Santhagopalan et al. [53] performed optimization of a wind turbine column by coupling RANS solver for predicting wind turbine wakes and turbulence. Dynamic programming was used by Santhagopalan et al. to estimate optimal tip speed ratio (TSR) and streamwise spacing of the turbines by using a mixed-objective performance index consisting of total power production from the entire turbine array with the penalty of the average turbulence intensity impacting over the rotor discs.

To recreate realistic atmospheric conditions, CFD solutions of the Navier-Stokes equations must be studied. A variety of complexities of studies exist in this field, from full LES simulations of diurnal planetary boundary layers (PBL) to two-equation (such as k-ε model) RANS simulations of neutral ABL boundary conditions. A discussion of select CFD studies is provided in the following section.

The first study investigated here is that of O’Sullivan et al. The study includes boundary conditions and wall functions used in ABL modelled. The researchers used a classic neutral ABL. When using a k-ε RANS turbulence model, frequently there are wall functions incorporated into the model to more accurately capture the near wall behaviour (Menter et al. [27]). Many errors can be avoided by selecting a wall function that is consistent with the profile being investigated. Most importantly, the interior of the profile must be in equilibrium with the profile calculated by the wall function (O’Sullivan, et al.). This issue of near wall modelled addressed by wall functions can be avoided by using a RANS model derived with wall bounded model in mind like the k-ω models (Menter et al. [26]).

It is a common practice to prescribe Neumann boundary conditions (e.g. zero-gradient fluxes) at the top of the boundary layer (O’Sullivan, et al. [31]). In ANSYS FLUENT this type of boundary is called a symmetry boundary condition. This is most frequently done to minimize the size of the domain. In ABL flow, however, the top boundary condition should allow for fluids to exit and re-enter the domain to account for vertical flows induced by objects. By their nature zero-gradient boundary conditions prevent vertical flows across the boundary. O'Sullivan et al. solved this problem by setting a constant shear stress at the top boundary since the top boundary is sufficiently inside the constant shear stress layer. The gradients can thus be calculated. This approach has the advantage of the zero-gradient models with the gradients calculated from the inflow profiles allowing for flow to enter and exit the domain.

The results of O'Sullivan et al. [31] show that the error associated with the proposed boundary conditions were of the same order as the convergence criteria, while the error associated with the zero-gradient boundary conditions caused the model to overestimate velocities up to four percent and underestimate turbulence intensities by as much as three percent. They also found that these errors held for models with much taller domains trying to account for the zero-gradient top boundaries.

Montavon et al. [62] performed another example of the use of k-ε RANS turbulence closure. In this study, a finite volume commercial CFD code, FLOW-3D, was utilized to model neutral and stratified flows over complex terrain. To achieve a model capable of handling stratified flows the conservation equation and buoyancy term was implemented with potential temperature. Conditions of hydrostatic dominance and non-hydrostatic dominance were studied to determine the importance of vertical inertia. The first geometry studied was a 3-D domain containing a 2-D theoretical bell-shaped mountain. The results were found to correlate closely to the solutions found using linear mountain wave theory. The last simulation performed was of the extreme wind event experienced in Boulder, Colorado in January 1972, where 60 mph winds were experienced. This model was initialized with measurements taken in Grand Junction, Colorado, 300 km upwind. The results compared respectably (Montavon et al. [62]). The two previous RANS studies were successful in simulating fairly simple ABLs, however, the neutral ABL is a simplification of ABL conditions experienced with an assumed constant vertical density. To achieve more accurate ABL conditions, more sophisticated LES models must be used. Saiki et al. studied two very stable ABL cases using a LES model with a modified two SGS model. The cases investigated were a fanning or layering case prone to pollutants spreading out and a case with the forming of a nocturnal low-level jet (LLJ) (Saiki, et al. [34]).

In the case of the fanning or layering of very stable ABL, Saiki, et al. [34] were unsuccessful, only obtaining a mildly stable ABL. They attribute this failure to the SGS turbulence model. As stability increases the dominant eddies become much smaller. This puts a considerable extra burden on the SGS model (Basu et al. [2]). To reasonably predict the strongly stable ABL, significant advances in SGS models need to be made.

In the case of the nocturnal LLJ, Saiki et al. were successful in recreating a previously established event (Blackadar et al. [4]). The study had reasonably well correlated surface mean velocity and temperature profiles for the nocturnal LLJ The modelling of convective and neutral ABLs has reached its maturity. However, the modelling of stable ABL is still a field on the cutting edge with only a handful of successful studies. The LES study by Basu et al. [2] used a locally averaged scale-dependent dynamic (LASDD) SGS model to describe a full diurnal ABL cycle. One of the current drawbacks of LES is its dependence on the SGS model to capture the effect of the small scale eddies that are not resolved. Since eddies become increasingly small in stable conditions, a lot of burden rests on the SGS model to account for these smaller eddies. By using the tuning-free (dynamically computed) LASDD SGS model, Basu et al. were able to better account for the SGS eddies. Other complications that arise when modelling both convective and stable ABLs are the domain size and grid size. To properly capture the convective ABL, a large domain is needed. However, for a stable ABL, fine grid resolution is required. This leads to a mesh size of the order 109 and an exceedingly small time step requiring massive computing power.

The objective of the study by Basu et al. was to determine if the LASDD SGS model was capable of modelling diurnal cycles inclusive of strongly stratified ABLs. To test this, they simulated day 33 and night 33/34 of the Wangara case study. The Wangara case study was performed in Hay, Australia in 1967. The location was a flat vegetation free area to reduce any topographical effects (Clarke, et al. [11]). The simulation run by Basu et al. was able to qualitatively reproduce the diurnal ABL cycle including the formation of a nocturnal LLJ in magnitude, direction and duration. However, the elevation of the LLJ was shallower than the one experienced in the Wangara experiment showing that the shear layer was under estimated. This under-prediction could be very critical when designing wind farms as a predicted shallow nocturnal LLJ could significantly impact a wind farm. As was found in earlier studies, Basu et al. (2008) also found that, the mixed layer temperature was slightly lower than the actual temperature experienced. However, it should be noted that radiant surface heating was not included in the model.

2.3 Power Curve

Predicting the power output of a wind turbine as a function of wind speed is very important. This is accomplished by developing specific power curves for each different wind turbine model. In these wind models there is a cut-in wind speed, in which any wind below the cut-in velocity does not create any power output. This is because of mechanical friction and aerodynamic losses that must be overcome before power can be generated. Variable pitch turbines start with high angles of attack so some stall is present. In addition, turbines start in a turbulent wake state so there are additional loses that must be overcome by a higher wind velocity prior to power generation. From the cut-in wind speed the power output rapidly increases and is proportional to as shown in Equation 2.13.

$$P = \frac{1}{2}\rho A[V_\infty]^3 \qquad 2.13$$

As the power approaches the rated power, it is necessary to implement controls to prevent the generator from absorbing more power than it is capable. This limitation is accomplished most frequently with blade pitch control by putting the turbine into a semi-stalled state to match the desired power output (Lesihman et al. [23]).

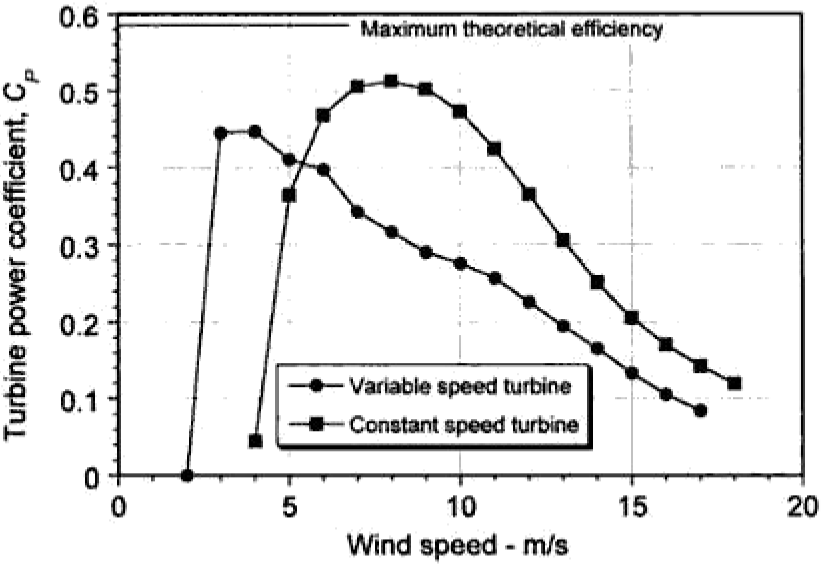

Figure 2.5 Representative power coefficient versus wind speed curves for constant speed and variable speed HAWTs [23].

Li Qing’an et al. [55] investigated the effect of solidity σ on wind turbine performances. Li Qing’ an. et al. tested 2 to 5 blade in straight-bladed VAWT in wind tunnel experiment. The power coefficients decrease with the increase of the solidity. However, the torque coefficients increase with the increase of solidity. For the solidity of σ = 0.084, 0.127, 0.169 and 0.211, the maximum values of power coefficient are about C_P = 0.211, 0.202, 0.195 and 0.184, respectively.

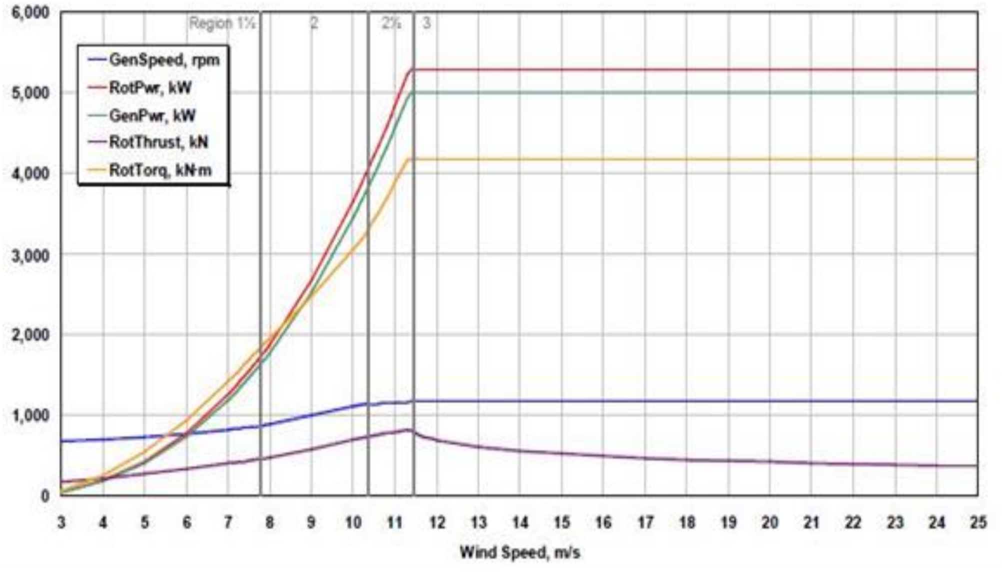

Figure 2.6 Power Curve for NREL 5MW reference turbine [22].

Gottschall et al. [15] have proposed a dynamic power curve. Rather than basing the power curve off of a ten-minute average wind speed like the International Electrotechnical Commission (IEC) code suggests, they split the wind speed into an average and a stochastic wind speed, much like the Reynolds decomposition widely used in turbulent flows. This allowed them to look at small time scale dynamics of power generation. Their dynamic formula to calculate power is:

$$\frac{d}{dt}P(t) = D^{(1)}(P;u) + \sqrt{D^{(2)}(P;u)\Gamma(t)} \qquad 2.14$$

Where $D^{(1)}(P;u)$ is the drift coefficient responsible for the average wind speed part of the equation, $D^{(2)}(P;u)$ is the diffusion coefficient which, when combined with the Langevin force,$\Gamma(t)$, is responsible for the stochastic aspect (Gottschall et. al. [15]). Figure 2.6 compares the exact power curve, the IEC power curve and dynamic power curve proposed by Gottschall et al. Thus conclude that their dynamic power curve cannot replace the IEC standard curve but is simply another way to look at power characteristics.

2.4 CFD Wind Turbine Model

Empirical models, like the BEM method, have played an important role in the development of the wind energy industry. However, as the industry continues to grow and prime farm sites become scarcer, resulting in higher density turbine placement, advanced CFD simulations will be required to meet demand and advance the industry (Bazilevs, et al. [3]). A variety of techniques and methods have been used to study wind turbine wake interactions (Hahm et al., [18]; Porté-Agel, et al. [37]; Tachos, et al. [37]), atmospheric wind farm effects (Calaf, et al., [9]; Meyers [28], and structural loads and spacing (Bazilevs, et al.; Meyers et al.). These studies range from using RANS turbulence closures (Hahm et al.; Tachos, et al.), to LES with a variety of SGS models (Bazilevs, et al.; Calaf, et al.; Meyers et. al [37]; Porté-Agel, et al., to a case using the vorticity transport model (VTM). The following Literature review will explore their studies and what can be learned from their methods and results.

Xin Cao et al. [56] simulated full scale HAWT for wind shear and yaw. The calculated wind turbine, which contains tapered tower, rotor overhang and tilted rotor shaft constructed by making reference of successfully commercial operated wind turbine designed by NEG Micon and Vestas. The blade produces the maximum aerodynamic loads when it is in the upwind region. While in the downwind region, the aerodynamic loads output drops significantly. The wind rotor produces positive yaw moment in the full rotation period.

Xin Shen et al. [59] proposed multi-objective optimization of wind turbine blades with sweep and dihedral 3-D shape. Lifting surface method with prescribed wake was used as the aerodynamics performance prediction model. Blade with 3-D shape can not only increase the power output of the rotor but also keep the thrust of rotor under control.

The effect of land scarcity in Germany with turbines spaced as close as has spurred increased regulation with respect to turbine fatigue. This increased regulation is based in rudimentary empirical calculations of turbulence intensity. A study by Hahm et al. [18] investigated the structure of turbulence intensity comparing their results to common empirical methods. Their study focused on the wake structure behind a single MW class turbine using both k-ε RANS model and a detached eddy simulation (DES) model. The empirical model investigated casts the turbulence intensity in the far wake as the sum of the upstream turbulence intensity and a bell-shaped turbulence intensity defined as a function of thrust coefficient and the tip-speed ratio. The results of their study gave an idealized modification to the empirical model by casting the additional turbulence intensity as three bell-shaped curves with the primary peaks aligned with the tip vortices. A comparison of the two models is provided in Figure 2.7.

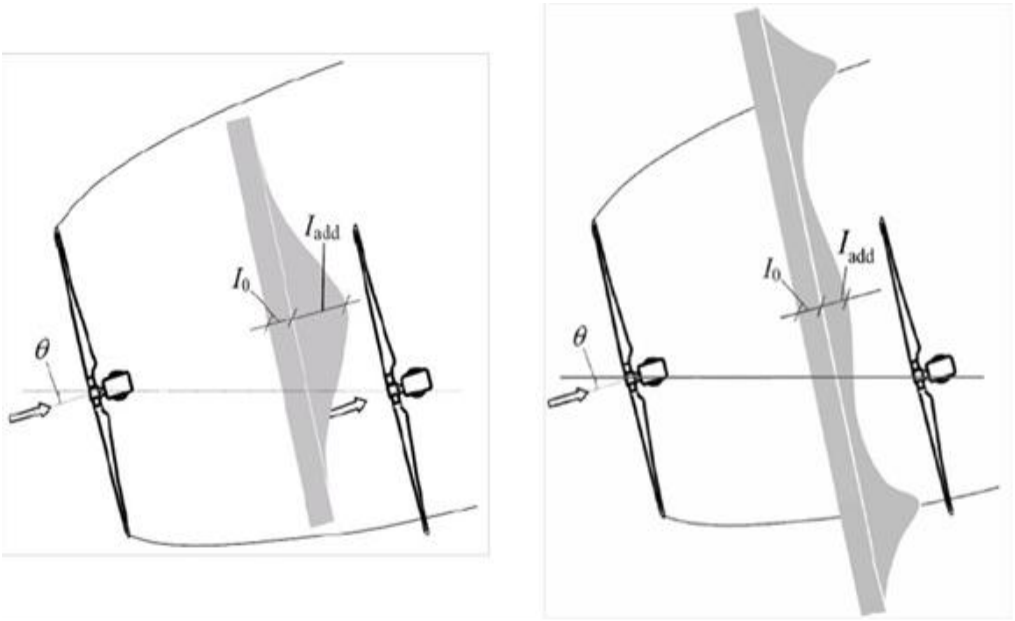

Figure 2.7 Distribution of turbulence intensity in wake for empirical model (left), and idealized results of CFD study (right) [18].

The k-ε RANS study simulated a previously studied 55kW turbine with a neutral ABL using a multiple reference frame model in FLUENT. Results were relatively successful at reproducing velocity profiles measurements downstream, yet due to the averaging nature of RANS models the turbulence intensities near the edges of the wake were under-predicted.

The DES simulation used a homogeneous ABL to model an ENERCON E66 turbine for which turbulence data was available. This model also produced relatively successful results. The error in the DES model was attributed to boundary influences from a limited domain size. This resulted in an under-prediction of turbulence intensity just outside the wake region.

Although Hahm et al. experienced some difficulties with the k-ε RANS closure model, other RANS closure models should be explored. Tachos et al. (2010) performed a parametric study of RANS closure models on the NREL Phase II wind turbine to determine the applicability of RANS closure models. The models used include Spalart-Allmaras (SA), k-ε, k-ε renormalization group (RNG), and the k-ω shear-stress transport (SST) closure models. The simulation was set up using a single blade from the NREL Phase II turbine in a single reference frame with 120° periodic boundary conditions. As a perspective of the size and computation time, the mesh was 4.2 million cells and the k-ω SST model took the equivalent of 20 days of central processing unit (CPU) time. The model run as steady state in FLUENT. The means of validation used by Tachos et al. [17] was pressure distribution on the blade surfaces. They found that the k-ω SST model had a very good correlation with measured values. The k-ε RNG and SA models had good correlation. The discorrelations found were determined to be a result of flow separation. The k-ε closure model performed very poorly, likely because of its lack of an explicit term to account for rotation. Overall, it concluded that because of the near wall formulation, the k-ω SST model was the most suited RANS turbulence closure model for wind turbine simulations.

Porté-Agel et al. [33] performed a LES study using a tuning-free Lagrangian dynamic SGS model recently developed for wind energy applications to model both single turbine wakes and wake interactions in an operating wind farm. Fully resolving a rotating wind turbine significantly increases CPU time and model complexity. As a means of simplifying the model and cost savings, an actuator disk model (ADM) can be implemented to act as a momentum sink with properties mirroring that of a wind turbine. Porté-Agel et al. studied three different actuator disk models. The first was a non-rotating actuator disk model (ADM-NR). For this model, the Rankine-Fronde actuator disk model was used for its widely accepted ability when using coarse grids. This model assumes that forces only act in the axial direction eliminating the ability for the model to capture rotation. For the ADM-NR, the force, F_x, is represented as,

$$F_x = \frac{1}{2}\rho \widehat{u_0^2 A C}_T \tag{2.15}$$

Where u_0 is the unperturbed resolved velocity of axial incident flow acting on the center of the disk, A is the swept area of the rotor, and C_T is the thrust coefficient. The second model used was a rotating actuator disk model (ADM-R). This model uses the BEM method described in section 2.1, integrated over the rotor disk to calculate 2-D forces. This results in the ability of the ADM-R to model rotation. However, because it is integrated over the area of the disk, it is not able to capture the tip vortices. The final model studied was an actuator line model (ALM). This model uses the BEM method to calculate turbine induced lift and drag forces, and evenly distributes them along the actuator lines. By using lines rather than a disk, the ALM is capable of capturing tip vortices and uses far fewer cells than resolving the actual turbine blades. The main advantage of using the actuator models is a reduced mesh size and subsequently reduced computational costs.

The actuator models were validated against a wind tunnel experiment Porté-Agel et al. performed using a 0.15 meter diameter wind turbine model and a log-law incident neutral ABL. As can be seen in Figure 12, the ADM-R and ALM models very closely align with the measurement in the near and far wake regions. The ADM-NR model underestimates the velocity deficit in the near-wake region but agrees quite well in the far wake region. The results of turbulence intensity were not as close. The ADM-R and ALM models both correlated very well with each other but only correlated reasonably well with the wind tunnel data. The ADM-NR on the other hand under-predicted the turbulent intensity across the board.

The operational wind farm, Porté-Agel et al. chose for this study is located in Mower County, Minnesota. Five turbines located in an outlying section upwind of the main farm chosen. Measurements made using a technique called sonic detection and ranging (SODAR). SODAR measures the vertical wind profiles using three beams offset 10° from vertical. Two SODAR instruments was utilized. One was placed in line with the first row of turbines. The second was placed about halfway between the first and second in-line turbines. Measurements were taken during a time when a neutral ABL was present. As a result, Coriolis and buoyancy were neglected in the CFD model. Once again very strong agreement was found between the measured velocity field and the ADM-R and ALM results behind the first turbine. Similar to the previous case, the ADM-NR under-predicted the velocity deficit behind the first turbine. Turbulence intensities were under-predicted across the board by 20%. Since no other SODARs were used, subsequent wake interactions could not be compared (Porté-Agel et al. [33]).

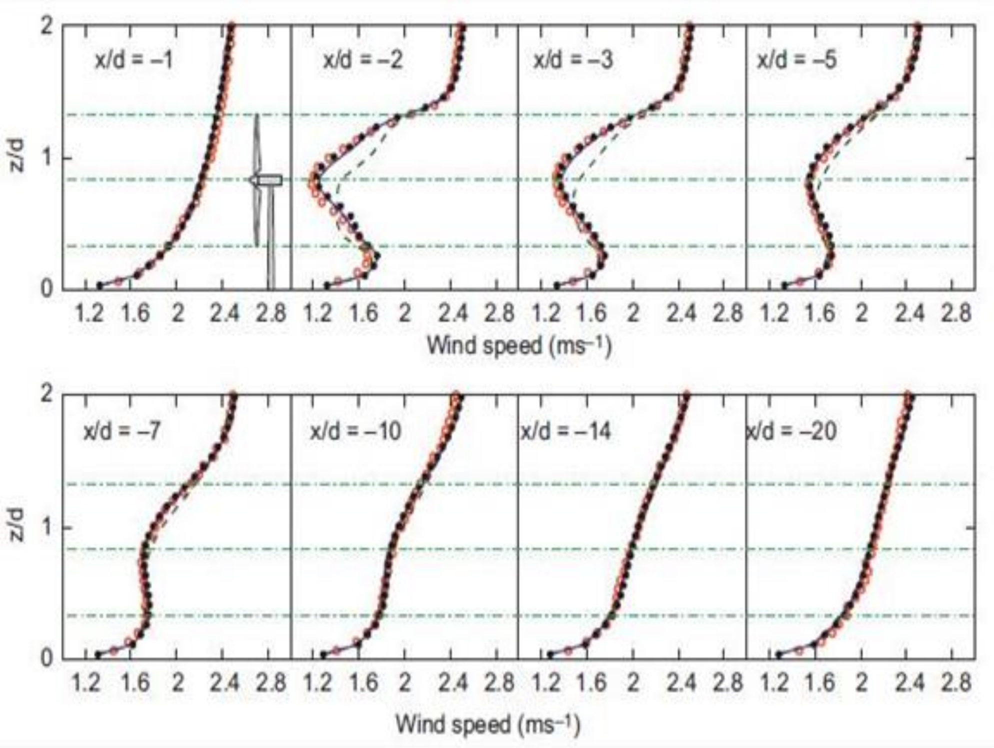

Figure 2.8 Streamwise velocity profiles (m/s): wind tunnel measurements, ADM-NR (dashed line), ADM-R (solid line), ALM (dotted line) [33].

Power deficits seen by the second turbine were also compared. It was noted that the actual power deficits experienced in the wind farm by the second turbine were between 47% and 50%. The ADM-R and ALM simulations both resulted in a power reduction of 48% whereas the ADM-NR simulation only resulted in a 37% power reduction. This was expected since the ADM-NR simulation significantly under-predicted the velocity deficit, as well .

As wind farms continue to grow in size it is conceivable that they may start to affect the ABL in a similar manner to heavy vegetation. Although this does not have much potential to significantly affect the larger PBL, it could have a significant effect on wind farm production (Calaf, et al., [9]).

Calaf et al. proposed that wind farm arrays exceeding 10-20 km in size approach the infinite wind farm asymptotic limit, causing the boundary layer flow to be almost in a fully-developed state. There are several models that have been developed for atmospheric studies to predict the modified ABL as a function of surface roughness. A comparison of two of these models, Frandsen et al. [14] was performed and a modification to the Frandsen formula was recommended. For their study, Calaf et al. developed a parametric study of wind farms using a LES model with a Smagorinsky SGS closure scheme. They modelled entire farms varying the number of turbines and spacing of those turbines. The setup of the study included the turbines as non-rotating actuator disks, and using a pressure forced neutral ABL.

Calaf et al. noted that in wind tunnel experiments performed by Frandsen et al., in which streamwise spacings of 7.85 and larger were used, significant velocity recovery occurred prior to the subsequent turbine. This was reflected in the results of the CFD study performed by Calaf et al., as well. It has been observed that when modelling single turbines, the energy comes from the difference in kinetic energy flux over the turbine. For an array of turbines the kinetic energy must be entrained from above. This is seen as a result of the vertical kinetic energy fluxes being of the same order of magnitude as the power extracted (Frandsen, et al.). It was also observed that the turbine spacing only contributed about 10% to the total power production and effective roughness length. It was concluded that velocity changes in the streamwise direction can be neglected, since relevant exchanges of energy occur as a result of vertical entrainment.

Subsequent modifications were made to the Frandsen et al. [14] ABL formulation to provide reasonable agreement with the CFD results. It was noted that a model resolving rotating blades would provide more accurate results. Due to computational restrictions this had to be avoided.

Wind turbine wake interactions are only the first half of the problem of understanding fatigue impacts on wind turbines, the second half of the problem is understanding the structural response to those fatigue loads. In a two-part study, the complete problem was studied using a LES model with a residual-based variational multiscale (RBVMS) formulation of the Navier-Stokes equations coupled with a linear elastostatic structural finite element method (FEM) model (Bazilevs, et al. [3]). For this simulation a full two-way coupling was established such that the deformation of the blades subsequently deformed the fluid domain at each time step allowing for a much more accurate capture of the fluid-structure interaction (FSI).

Validation for their fluid model was performed as a simulation of a Taylor-Couette flow. This flow consists of two concentric cylinders with the outer cylinder stationary and the inner cylinder rotating. The problem captures elements of rotation, curved walls, boundary layer, and time-dependent evolution of velocity pressure fields. Results are compared to a DNS simulation for a Reynolds number of 8000, computed with 256 Fourier modes. Bazilevs et al. note that this only constitutes a partial validation of their model. To test their models, both a linear FEM and quadratic non-uniform rational B-splines (NURBS) solutions were calculated with constant grid size so the boundary was not resolved. Their results showed very close agreement of both models with the DNS data for the near wall region, with the boundary layer contained in the first cell. The NURBS solution was in much closer agreement through the middle region. However, the FEM solution did agree reasonably well.

In the study performed by Fletcher et al. [13], the wake influence of in-line turbines with spacings varying between 2D and 8D were studied. They also studied turbines offset by 0.5D and 1D with and axial spacing of 2D. No ABL was used and the ground was not included in the study. To model the turbines, a BEM formulation of actuator lines was implemented. They found that even with spacings of 6D, power losses of 40% to 50% were still experienced. They also found that oscillations in the power coefficient increased as the spacing between turbines increased due to the wake structure and dissipation.

2.5 Summarizing Remarks

As these case studies illustrate, there are many different numerical solutions to the Navier-Stokes equations that have been implemented successfully. Of the RANS closure models, the k-ω SST model was seen to have the most success. With respect to LES, the tuning-free SGS models were the most widely used. However, LES requires a very fine grid resolution to not over burden the SGS model. A method to mitigate large mesh sizes is the widely used actuator disk model. A variety of ADMs exist, but the best results were found among those formulated using the BEM method over a disk or actuator lines. To understand the larger picture of wake interactions and power losses, the entire wind farm must be modelled, however much is lost in the specific interaction of individual turbines. The interaction of just two turbines must be modelled for this purpose.

CFD modelled has come a long way in the past couple decades and has made great progress in the field of wind energy. In the most ideal simulation, the entire farm of fully resolved, rotating turbines would be with a very fine grid, and the solution would be achieved using LES with a tuning-free SGS model. However, computational capabilities have not achieved a level able to handle this problem and as a result, simplifications to the models must usually be made. Some wake structures and rotational effects were not captured in ADM studies even with LES grid resolutions. To capture the rotating effects of the wake, it is may be better to use a coarser RANS simulation that fully resolves the rotating turbine, than to use a finer ADM LES simulation. The current thesis work is directed toward addressing this hypothesis.

CHAPTER 3

PARAMETRIC STUDY

The research discussion which follows explores the velocity deficit effect created by turbine wakes through a suite of RANS models in ANSYS FLUENT. The geometry set used is GE 1.5xle.

Figure 3.1 Three blade GE 1.5xle [50]

The objective of this study to cross verify the lift force and drag force generated for different angle of attack and Reynold number, and to obtain the optimum angle of attack to work in order to get higher efficiency of wind turbine power generation. Determining the behaviour of these turbulence models for simplified turbine scenarios allows for a more educated selection of turbulence model when moving to a more sophisticated model (i.e. high resolution rotating model). All models were run on a four parallel processor system to demonstrate the capabilities of RANS models on non-supercomputer systems.

3.1 Fundamental Equations

The governing equations of fluid flow represent mathematical statements of the conservation laws of physics:

- The mass of a fluid is conserve.
- The rate of change of momentum equals the sum of forces on a fluid particle (Newton's second law).
- The rate of change of energy is equal to the sum of the heat rate added to a fluid particle and the work done on it (first law of thermodynamics).

These conservation laws are applied to a small fluid element, or control volume, by the Navier Stokes equations.

3.1.1 Navier Stokes

The theoretical basis for the problems of interest evolves from the conservations of mass (Equation 3.1) and momentum (Equation 3.2), represented by Pope et .al [32] as:

$$\frac{\partial \rho}{\partial t} + \nabla . (\rho \vec{v}) = 0 \qquad 3.1$$

$$\rho \frac{DU_j}{Dt} = \frac{\partial \tau_{ij}}{\partial x_i} - \rho \frac{\partial \Psi}{\partial x_j} \qquad 3.2$$

Where, $\vec{v}$ is the three-dimensional velocity vector, $\partial \tau_{ij}$ is the stress tensor, and Ψ is the external body force vector (in this case the gravitational potential). Nonlinearities prevent the direct numerical solution to these Navier-Stokes equations and indicate the use of the assumption of the turbulent viscosity theory. These instantaneous momentum and continuity equations can be written in an averaged form with the substitution of the Reynolds decomposition as,

$$U(x,t) = \{U(x,t)\} + u(x,t) \qquad 3.3$$

where, the x vector represents the streamwise x direction, the spanwise y direction, and the vertical z direction . The stress tensor is represented by Equation 3.4,

$$\tau_{ij} = P\delta_{ij} + \mu(\frac{\delta U_i}{\delta x_j} + \frac{\partial U_j}{\partial x_j}) \qquad 3.4$$

Where P is the pressure, δ_{ij} is the Kronecker delta, and μ is the molecular viscosity.

3.1.2 Standard k-ε model

The k-ε turbulence model is named for the two quantities that are being solved, the turbulent kinetic energy κ and the turbulent dissipation rate ε (Jones et al. [63]). It is classified as a two-equation model to reflect the two additional PDEs that are required to solve for the turbulent viscosity. It is the most common turbulence model in use (Pope et. Al., [32]). The transport equations as represented in ANSYS FLUENT are:

$$\frac{\partial}{\partial t}(\rho k)+\frac{\partial}{\partial x_i}(\rho k u_i)=\frac{\delta}{\delta x_i}\rho\left[\left(\nu+\frac{\nu_T}{\sigma_k}\right)\frac{\delta k}{\delta x_j}\right]+G_k+G_b-\rho_{\in}-\gamma_M+S_k \qquad 3.5$$

$$\frac{\partial}{\partial t}(\rho\varepsilon)+\frac{\delta}{\delta x_i}(\rho\varepsilon u_i)=\frac{\delta}{\delta x_j}\rho\left[\left(\nu+\frac{\upsilon_T}{\sigma_\varepsilon}\right)\frac{\delta\varepsilon}{\delta x_j}\right]+C_{1\varepsilon}\frac{\varepsilon}{k}(G_k+C_{3\varepsilon}G_b)-C_{2\varepsilon}\rho\frac{\varepsilon^2}{k}S_\epsilon \quad 3.6$$

In Equations 3.5 and 3.6, G_k and G_b are the kinetic energy production terms due to the mean velocity gradients and buoyancy respectively. The contribution from the fluctuating dilatation in compressible turbulence to the overall dissipation rate is Y_M. The turbulent Prandtl numbers for and are represented by the constants k and ε, respectively. $C_{1\varepsilon}$, $C_{2\varepsilon}$, and $C_{3\varepsilon}$ are constants and S_k and S_ε are source terms defined by the user. The turbulent viscosity is subsequently model using Equation 3.7

$$\upsilon_T=C_\mu\frac{k^2}{\varepsilon} \qquad 3.7$$

Where $C_{\underline{\mu}}$ is a constant.

The standard k-ε model is known to perform well in free shear layers away from boundaries and wake regions (Menter et. Al. [27]), but breaks down in boundary layers with strong pressure gradients. These issues originate in the turbulent viscosity hypothesis and the equation for . Modifications to the constants can yield better results but these solutions are generally considered to be very ad hoc.

3.1.3 Standard k-ω model

The standard k-ω model as originally developed by Wilcox [64] uses transport equations of k, the turbulence kinetic energy and ω, the turbulence frequency to solve for the turbulent viscosity (Menter et.al., [26]). These transport equations are:

$$\frac{\partial}{\partial t}(\rho k)+\frac{\partial}{\partial x_i}(\rho k u_i)=\Gamma_k\frac{\delta k}{\delta x_j}+G_k-Y_k+S_k \qquad 3.8$$

$$\frac{\partial}{\partial t}(\rho\omega)+\frac{\partial}{\partial x_i}(\rho\omega u_i)=\Gamma_\omega\frac{\delta\omega}{\delta x_j}+G_k-Y_\omega+S_\omega \qquad 3.9$$

Where G_k and G_ω represent the production terms from the mean velocity gradients and ω, respectively. And are the effective diffusivity of and, respectively. And are the dissipation due to turbulence from and, Similar to the k-ε closure models, and are user-defined source terms. The turbulent viscosity is model by:

$$\mu_t = a^* \frac{\rho k}{\omega} \tag{3.10}$$

$$\Gamma_k = \mu + \frac{\mu_t}{\sigma_k}$$

$$\Gamma_\omega = \mu + \frac{\mu_t}{\sigma_\omega}$$

$$a^* = a^*_\infty \frac{a^*_0 + {}^{Re_t}/_{R_k}}{1 + {}^{Re_t}/_{R_k}}$$

$$Re_t = \frac{\rho k}{\mu \omega}$$

R_k=6

Moreover, for high Reynolds number flow $a^* = a^*_0 = 0$.

3.1.4 k-ε RNG model

The k-ε RNG model developed with the statistical technique known as renormalization group theory (RNG). It based on the fundamental assumption of the universality of small scales in turbulence, as first suggested by Kolmogorov (Orszag, et al. [30]). The transport equations for k and ε in the k-ε RNG model are:

$$\frac{\partial}{\partial t}(\rho k) + \frac{\partial}{\partial x_i}(\rho k u_i) = \frac{\delta}{\delta_j}(a_k \mu_{eff} \frac{\delta k}{\delta x_j}) + G_k + G_b - \rho_\in - \gamma_M + S_k \tag{3.11}$$

$$\frac{\partial}{\partial t}(\rho \varepsilon) + \frac{\delta}{\delta x_i}(\rho \varepsilon u_i) = \frac{\delta}{\delta_j}\left(a_k \mu_{eff} \frac{\delta k}{\delta x_j}\right) + C_{1\varepsilon}\frac{\varepsilon}{k}(G_k + C_{3\varepsilon} G_b) - C_{2\varepsilon}\rho \frac{\varepsilon^2}{k} - R_\varepsilon + S_\varepsilon \tag{3.12}$$

It should be noted that there is a differential formulation of effective viscosity which account for effects of low Reynold numbers in near wall regions. For high Reynold number flow, turbulent viscosity calculated in the same manner as the standard k-ε models.

3.1.6 k-ω SST model

The k-ω Shear-Stress Transport (SST) model blends the strength of the standard k-ω and k-ε models and borrows the shear stress term from the Johnson-King model (Menter et. Al., [27]). By doing this, the k-ω SST model performs very well in the viscous sublayer and far wall regions. This is accomplished by the addition of blending functions that are zero away from the boundary resulting in a k-ε type model and one inside the boundary layer resulting in a k-ω model (Menter et. Al., [26]). It was mainly developed for flows with adverse pressure gradients and flows with separation. The transport equations for the k-ω SST model are:

$$\frac{\partial}{\partial t}(\rho k) + \frac{\partial}{\partial x_i}(\rho k u_i) = \Gamma_k \frac{\delta k}{\delta x_j} + \mathcal{G}_k - Y_k + S_k \qquad 3.13$$

$$\frac{\partial}{\partial t}(\rho \omega) + \frac{\partial}{\partial x_i}(\rho \omega u_i) = \Gamma_\omega \frac{\delta \omega}{\delta x_j} + G_\omega - Y_\omega + D_\omega + S_\omega \qquad 3.14$$

$D_\omega$is the cross-diffusion term used as a final blending term of the diffusion between the k-ω and k-ε models. The shear stress transport (SST) k-ω model was developed to effectively blend the robust and accurate formulation of the k-ω model in the near wall region with the free stream independence of the k –ε model in the far field [19]. The SST k-ω model is similar to the standard k-ω model, but it includes a number of features that makes the SST k-ω model more accurate and reliable for a wider class of flows than the standard k-ω model. The SST k-ω model does produce a bit too large turbulence levels in regions with large normal strain, like stagnation regions with strong acceleration. One of the main differences between the k –ε model and the k-ω based SST model is the eddy viscosity,

3.2 Model Description

The geometry of the GE 1.5xle [50] reference turbine was created in SolidWorks. This geometry was then exported into ANSYS DesignModeler, where the domain geometry was created. GE’s 1.5 MW wind turbine is the most widely used turbine in its class. The deformation due to aerodynamic loading of a wind turbine blade is performed is shown using a steady-state 1-way FSI (Fluid-Structure Interaction) analysis. The blade is 43.2 meters long and starts with a cylindrical shape at the root and then transitions to the airfoils S818, S825 and S826 for the root, body and tip, respectively. This blade also has pitch to vary as a function of radius, giving it a twist and the pitch angle at the blade tip is 4 degrees. The turbulent wind flows towards the negative z-direction.

Table 3.1 Technical data of GE’s 1.5xle [50]

Rated Capacity	**1500W**
Cut-in Wind Speed	3.5m/s
Cut-out Wind Speed	20m/s
Rated Wind Speed	11.5m/s
Electrical Interface	
Frequency	50/60 Hz
Voltage	690V
Rotor	
Rotor Diameter	82.5m
Swept area	5346m^2
Tower	
Hub Height	80m

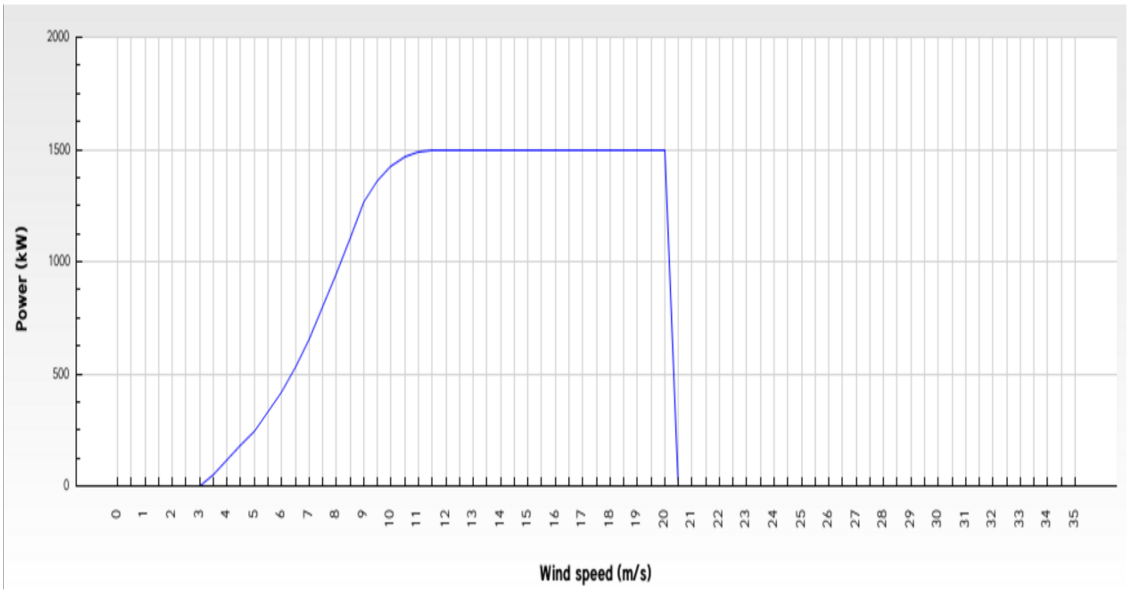

Figure 3.1 GE’s 1.5xle Power vs Speed [50]

Figure 3.1 shows how power varies with the change of speed in GE’s 1.5xle blade. From this, we can infer that 12 m/s to 20 m/s will give us maximum power.

CHAPTER 4

METHODOLGY

4.1 CFD Modelling Overview

CFD is a way of modelling complex fluid flow by breaking down geometry into cells that comprise a mesh. At each cell an algorithm is applied to compute the fluid flow for the individual cell. Depending on the nature of the flow either the Euler or Navier-Stokes equations can be used for the computation.

Step 1: Problem Identification

- Define goals
- Identify domain

Step 2: Pre-processing

- Geometry
- Mesh
- Physics
- Solver setting

Step 3: Solve

- Compute solution

Step 4: Post-processing

- Examine results

4.1.1 Model generation

Wind turbine blade of GE’s 1.5xle was generated in Solid works software using the coordinate from [12]. Solid Work is modelling software. Generated model was imported in Ansys 15.0. Blade model is shown in figure 4.1

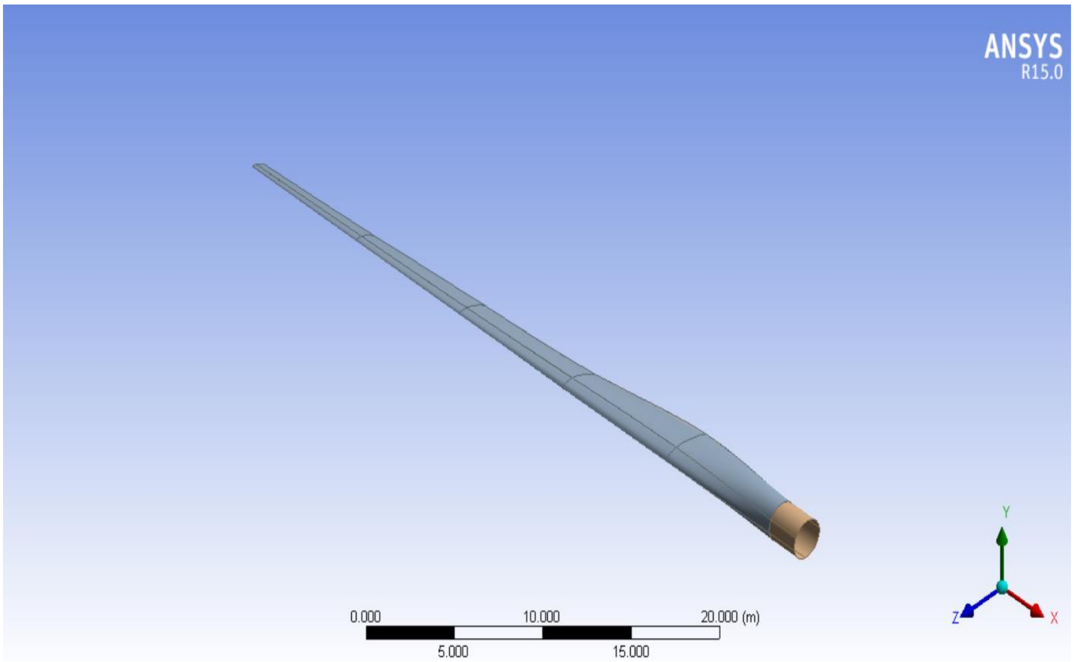

Figure 4.1 Geometry of GE’s 1.5xle

4.2 Mesh Generation

A discretization scheme involves breaking down a geometry into smaller parts, such as elements, nodes or volumes. The resulting discretized geometry, which is now a group of several smaller computational regions, is termed a grid or a mesh.

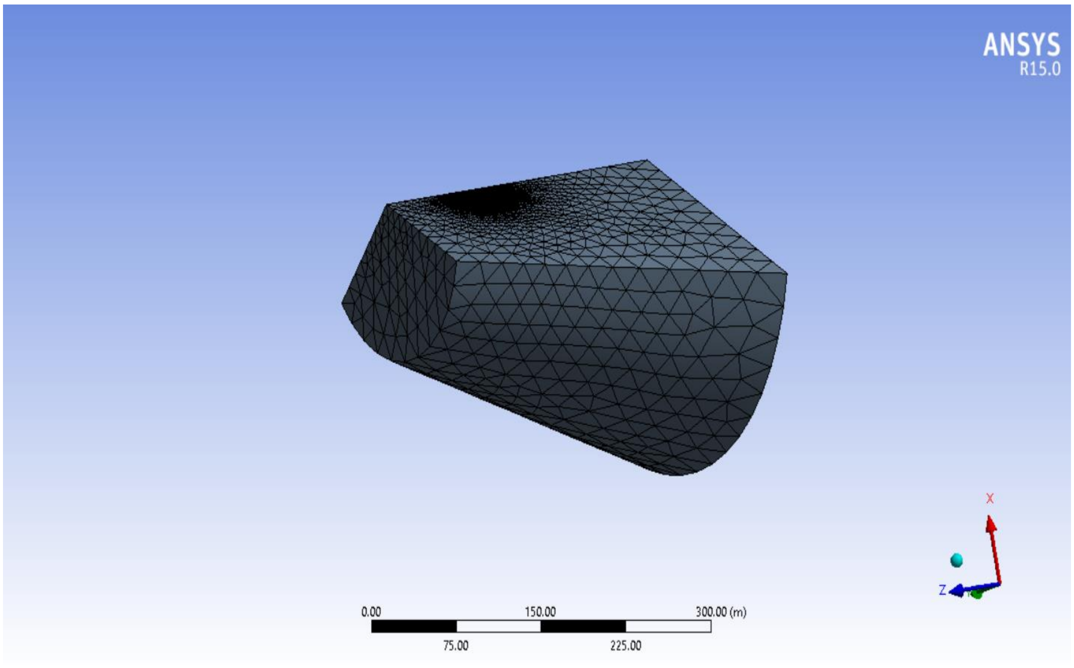

Figure 4.2 Tetrahedral Mesh

The accuracy of the simulation usually increases with increasing number of cells, i.e. with decreasing cell size. However, due to limitations imposed by the increased computer storage and run time some compromise in mesh size is nearly always inevitable. Fluent-Mesh creates linear tetrahedron, hexahedron and wedge/prism element shapes.

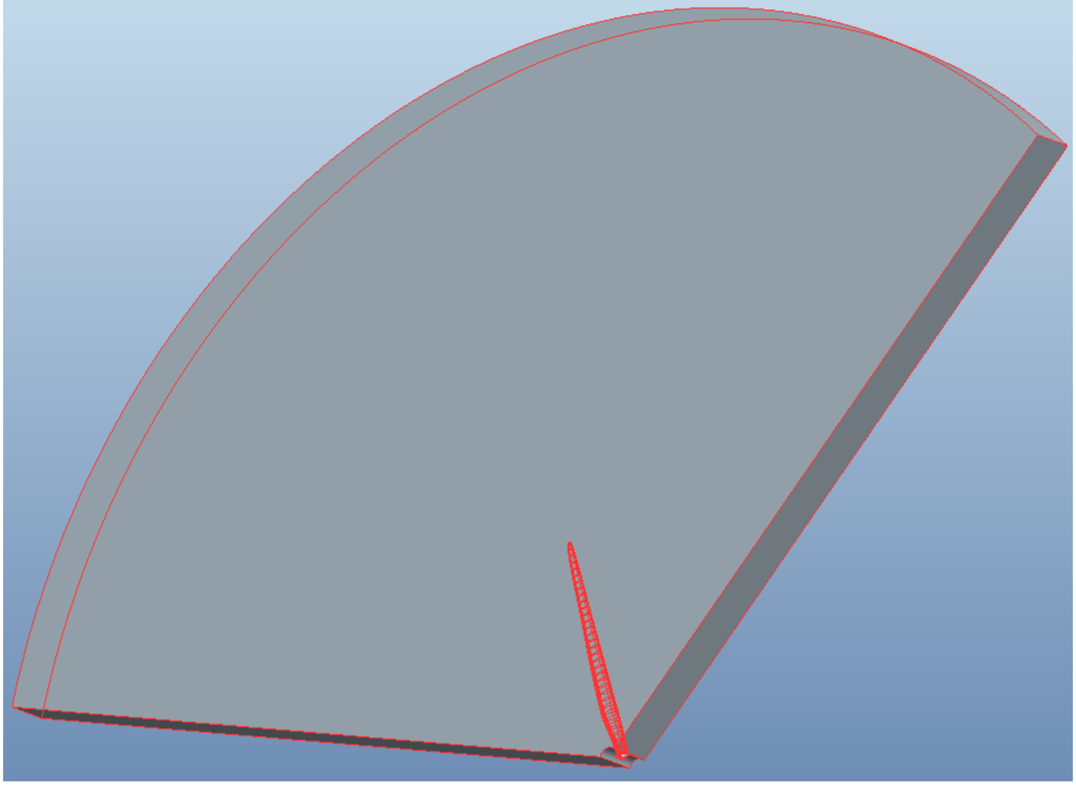

Figure 4.3 Curved out GE’s 1.5xle blade.

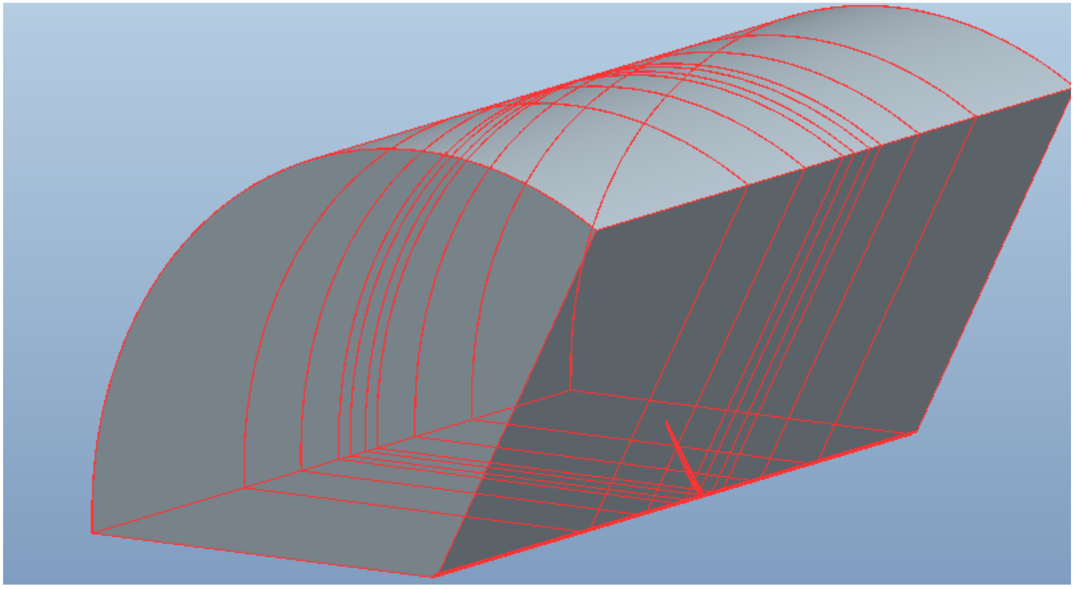

Figure 4.4 Tunnel resembling the surrounding of Wind Turbine.

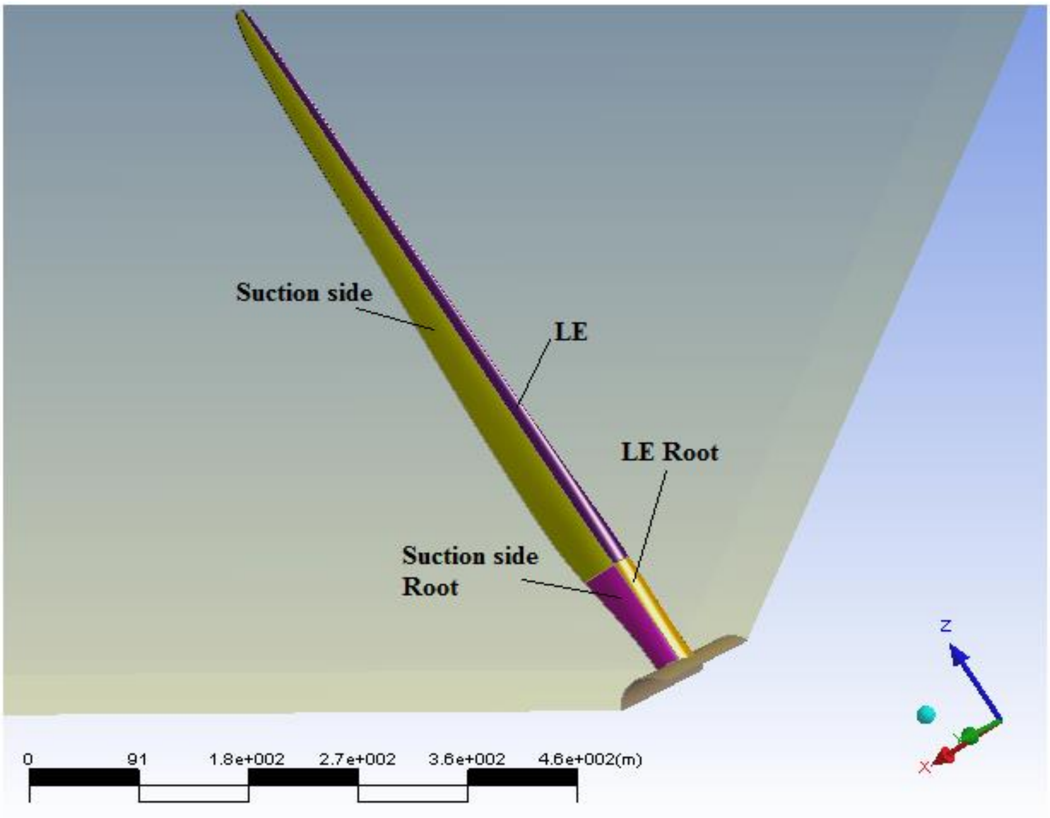

Figure 4.5 Section of blade

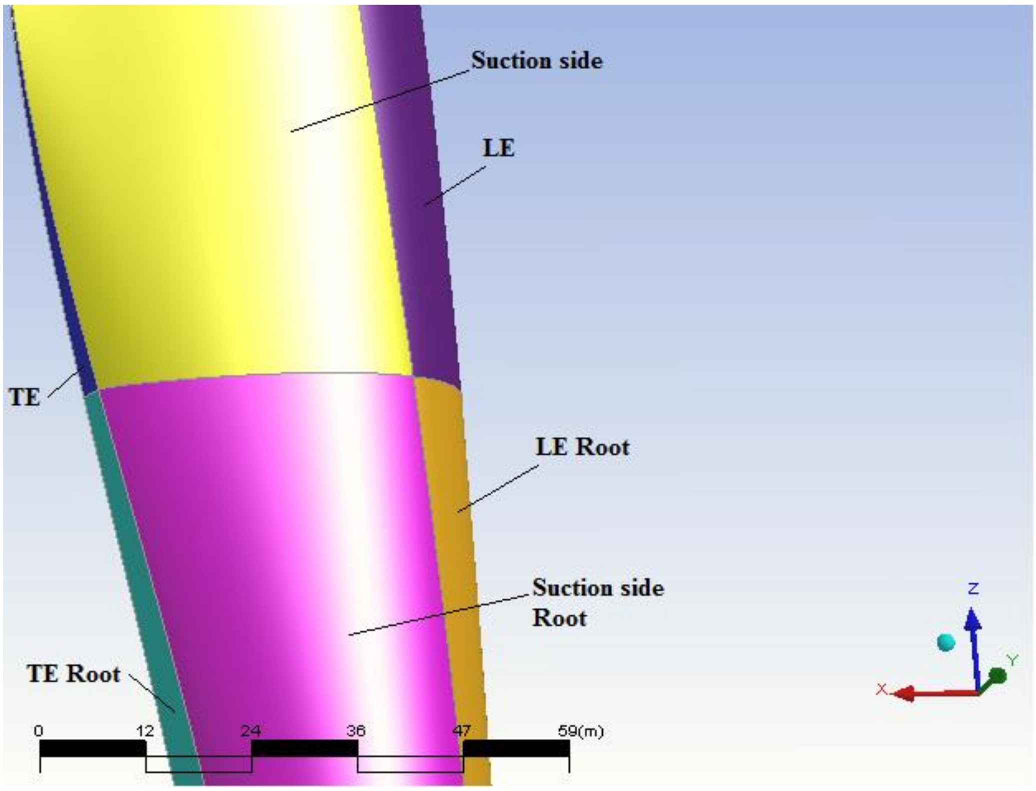

Figure 4.6 Close up of section of blade

All the different regions had different cell size limits, these can be viewed. The blades were divided into 8 different regions; leading edge, LE, trailing edge, TE, suction side, pressure side, suction/pressure side for the root, LE and TE for the root and then the tip.

4.3 Wind Turbine Simulation/setup

All simulations consist of two parts, one tunnel “stator”, and curved out blade “rotor”.

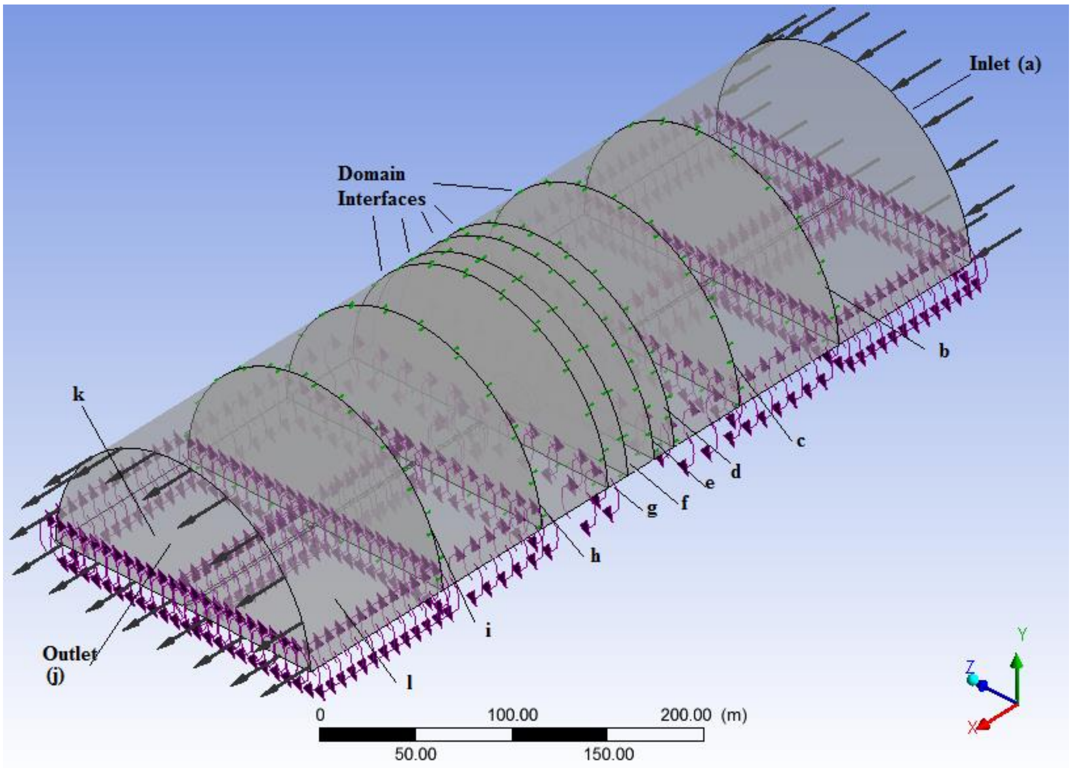

Figure 4.7 Stator region of blade

The different interfaces between the regions in the stator and rotor, have been listed (Table 4.1).The interfaces between the 3D regions are called faces.

Table 4.1 Different interfaces in stator and rotor

Face	Domain Interface
A	Velocity inlet
b,c,d,e,f,g,h,i	General Connection
J	Pressure outlet
k,l,m,n	Rotational Periodicity
o,p,q	General Connection

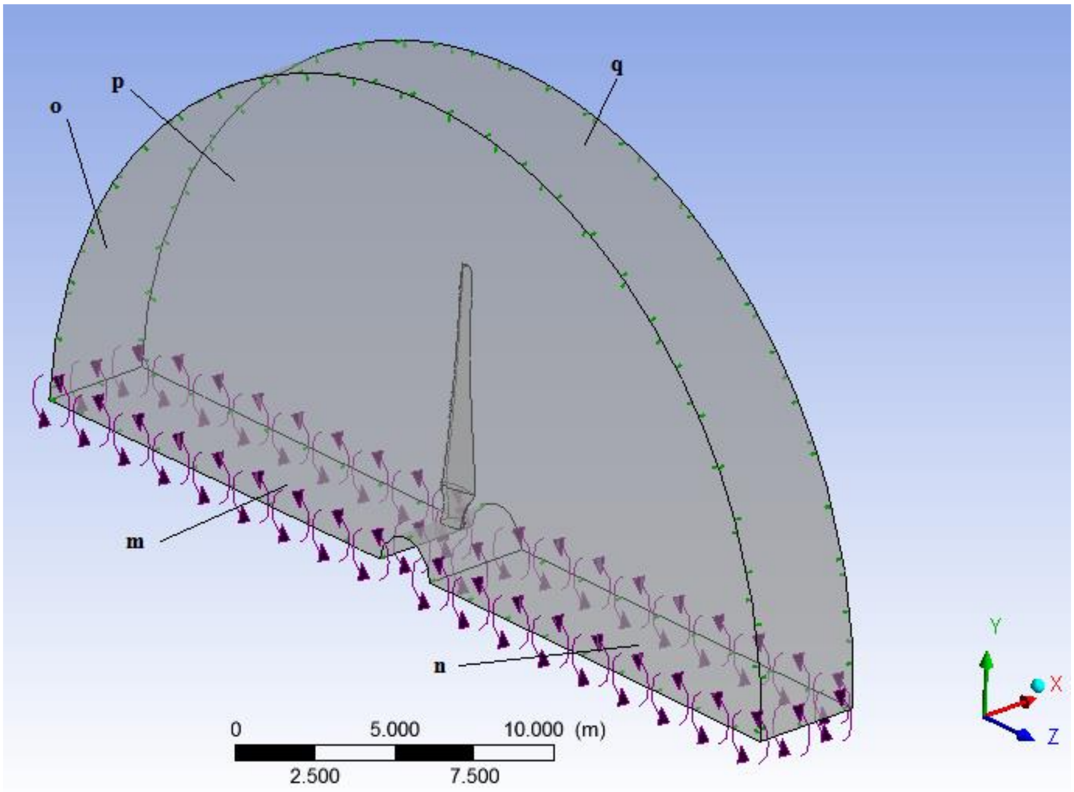

Figure 4.8 Rotor region of blade

Domain k and l covers each half of the entire underside of the stator in all 9 regions. The rotational periodicity means that whatever comes out of domain k comes into domain l. This makes it possible to cut the domain in half and save many nodes in the mesh. In case 1 the stator and rotor domains are 120^0 degrees because we are operating with a 3 bladed turbine, see Figure 4.3. The general connection which is most frequently used in Table 4.1 lets fluid pass from one region to another regardless direction and magnitude of velocity and pressure. At the velocity one specifies among other things the inlet velocity, turbulence intensity and pressure.

In the simulations double precision is used due to the large difference in element size close to the blade compared to further away from the blade.

4.4 Numerical Setup

Summary of step

1. Solution Methods
    - (a) Change Scheme to Coupled
    - (b) Pressure to Standard
    - (c) Check Pseudo Transient and High Order term relaxation

2. Monitors
    - (a) Change the residuals of each field to 1e-6
    - (b) Create a surface monitor
    - (c) Select plot
    - (d) Select write
    - (e) Select Blade surface
3. Solution Initialization
    - (a) Standard
        - i. From inlet
4. Run Calculation
    - (a) Set the number of iterations to 1500
    - (b) Initialize and Run calculation

CHAPTER 5

RESULT AND DISCUSSION

5.1 Validation

Validation of result done with the experimental result of wind turbine blade [52] for Reynold number 6000000, 3000000, and 250000 at angle of attack 5^0, 15^0, and 25^0.

Figure 5.1 Validation for Angle of attack vs Coefficient of Drag at Re= 600000

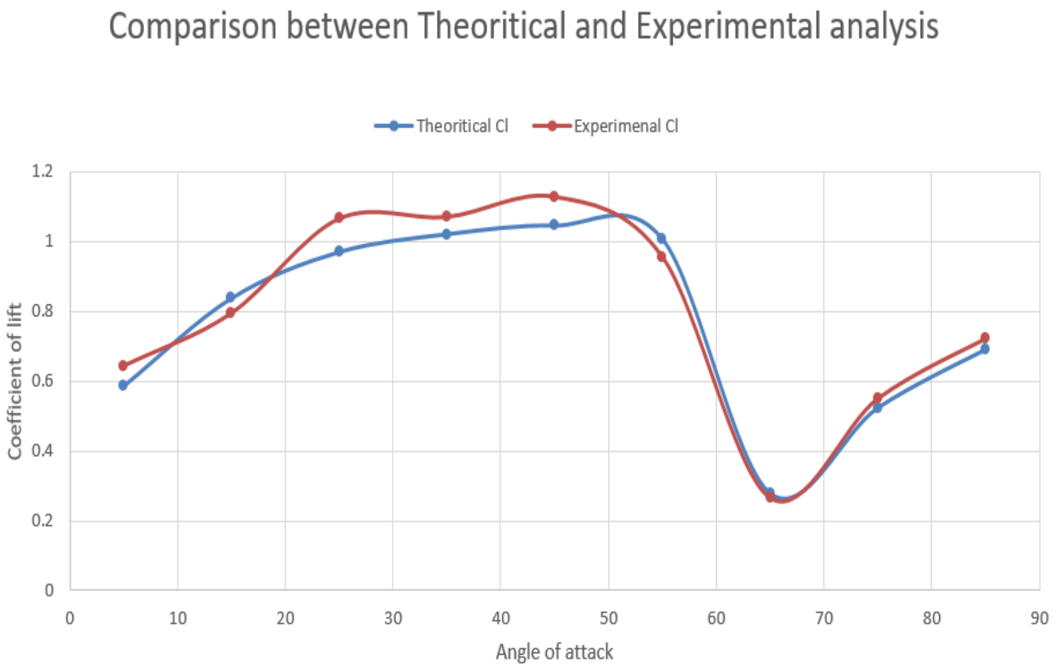

Figure 5.2 Validation for Angle of attack vs Coefficient of lift at Re= 600000

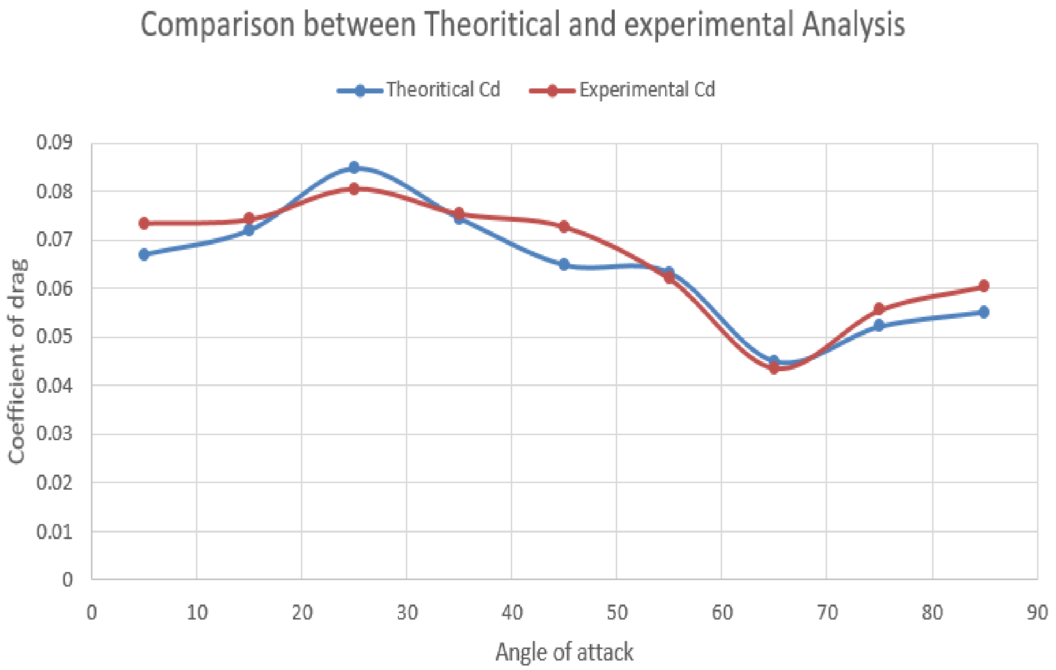

Figure 5.3 Validation for Angle of attack vs Coefficient of Drag at Re= 300000

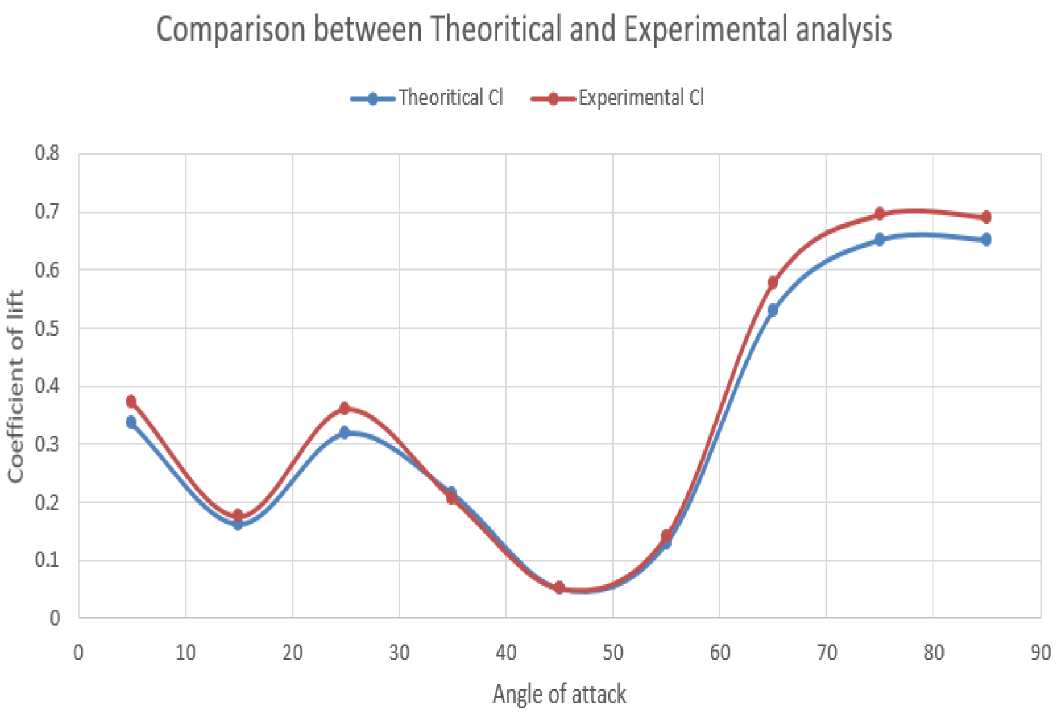

Figure 5.4 Validation for Angle of attack vs Coefficient of lift at Re= 300000

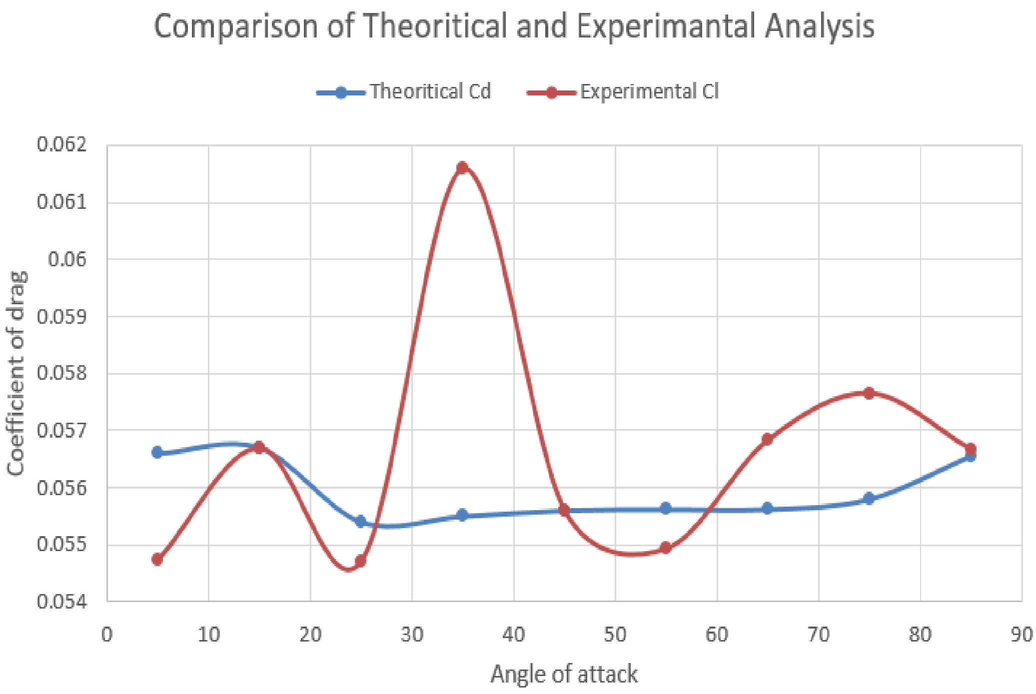

Figure 5.5 Validation for Angle of attack vs Coefficient of drag at Re= 250000

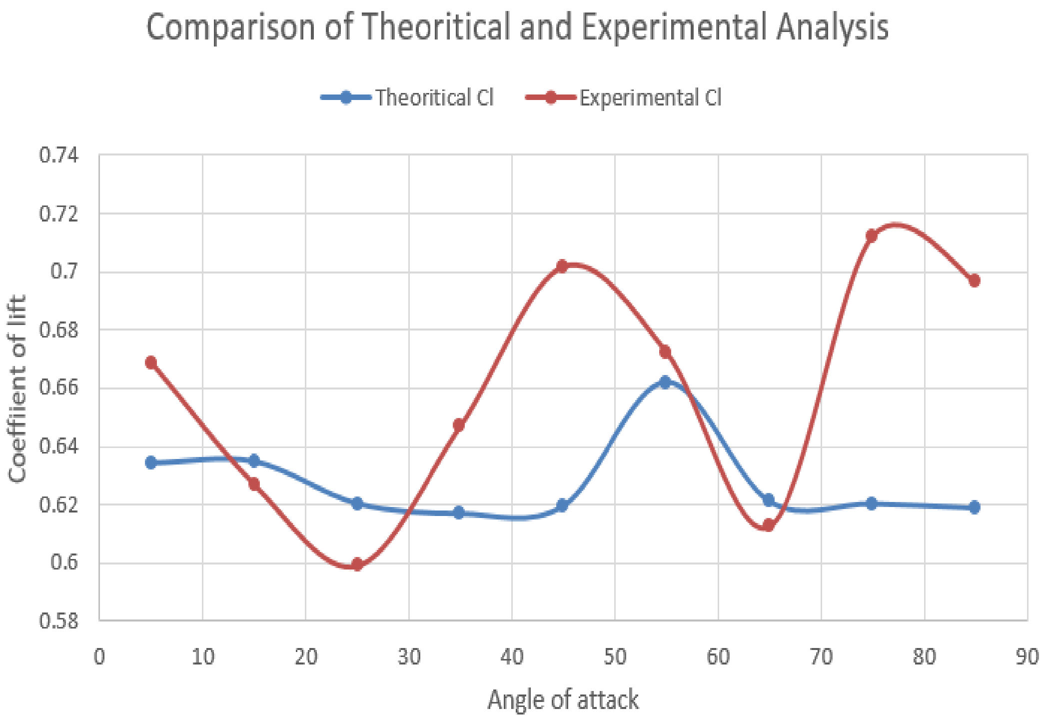

Figure 5.6 Validation for Angle of attack vs Coefficient of lift at Re= 250000

5.2 Result

As discussed in above chapter simulations of wind turbine blade done for a particular Reynold number for different angle of attack like 5^0, 15^0, 25^0, 35^0, 45^0, 55^0, 65^0, 75^0, 85^0. Likewise, six set of simulation done for different Reynold number like 12500, 125000, 250000, 500000, 3000000, and 6000000. This result is as shown below in table.

Table 5.1 C_d and C_l at various angle of attack at Re=12500

S. No	Angle of Attack	C_d	C_l	C_l/ C_d
1	5	0.05466	0.6079	11.12
2	15	0.05463	0.6073	11.11
3	25	0.05493	0.61336	11.28
4	35	0.05657	0.6216	10.98
5	45	0.05652	0.6211	11.01
6	55	0.05462	0.6058	11.09
7	65	0.05455	0.60677	11.23
8	75	0.05687	0.6198	10.89
9	85	0.05688	0.6199	10.90

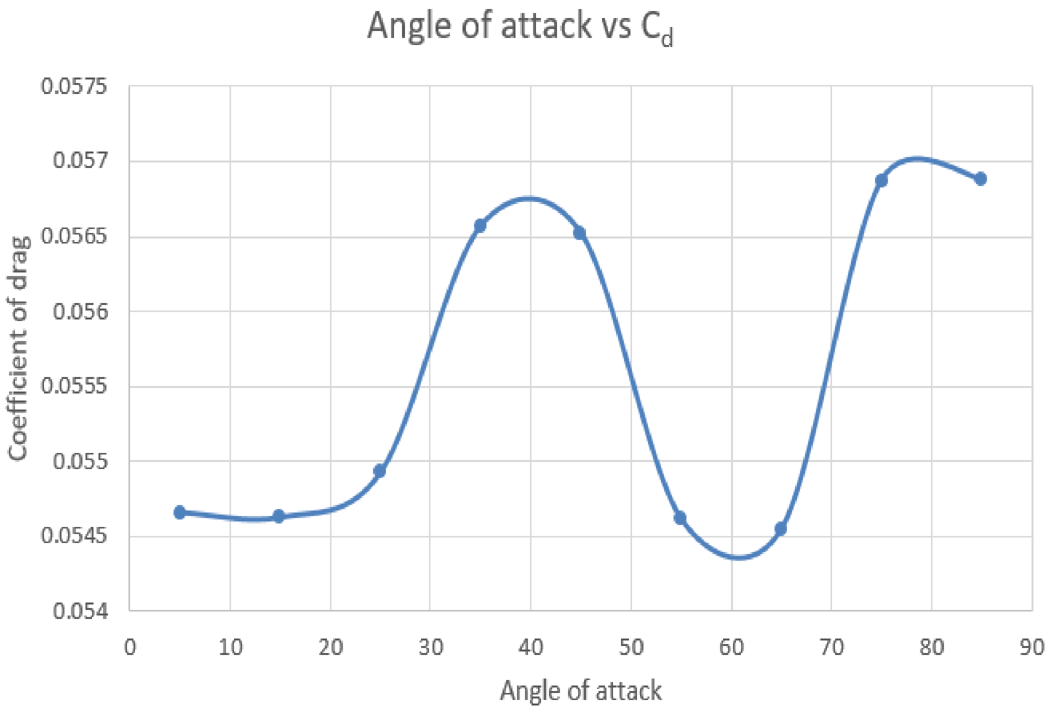

Figure 5.7 Graph between Angle of attack vs C_d for Re= 12500

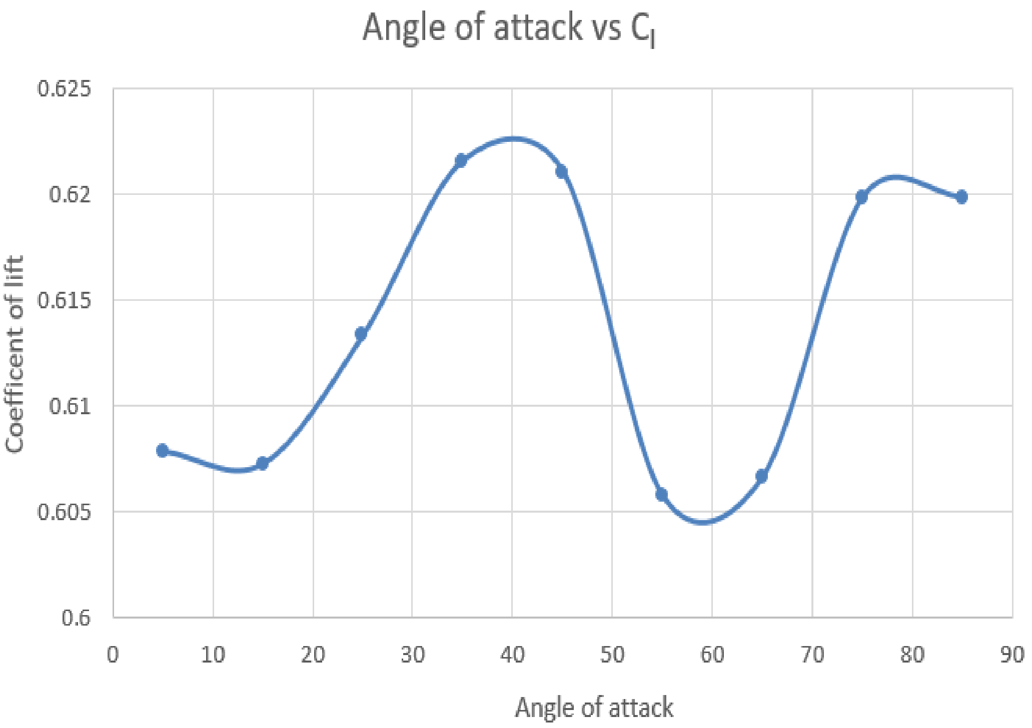

Figure 5.8 Graph between Angle of attack vs C_l for Re= 12500

Table 5.2 C_D and C_L at various angle of attack at Re=25000

S. No.	Angle of attack	C_d	C_l	C_l/ C_d
1	5	0.05488	0.6125	11.17
2	15	0.0559	0.6421	11.48
3	25	0.0549	0.6136	11.17
4	35	0.054972	0.61496	11.20
5	45	0.05497	0.61428	11.17
6	55	0.05495	0.6128	11.15
7	65	0.05478	0.6097	11.09
8	75	0.0541	0.6074	11.22
9	85	0.0543	0.6025	11.09

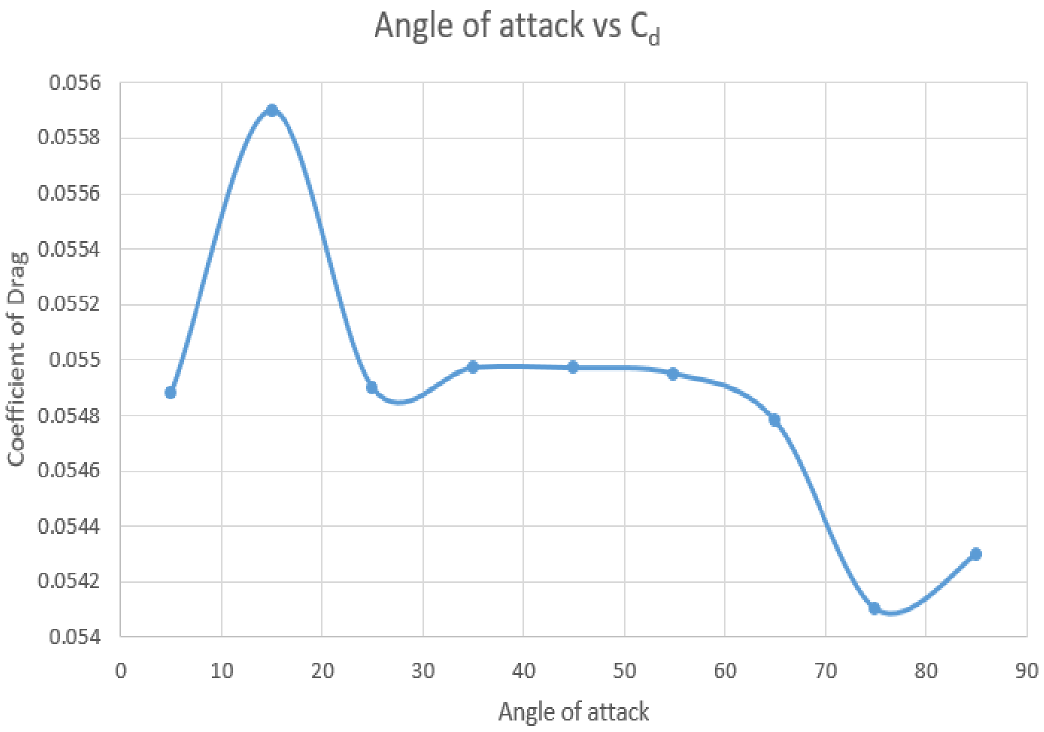

Figure 5.9 Graph between Angle of attack vs C_d for Re= 25000

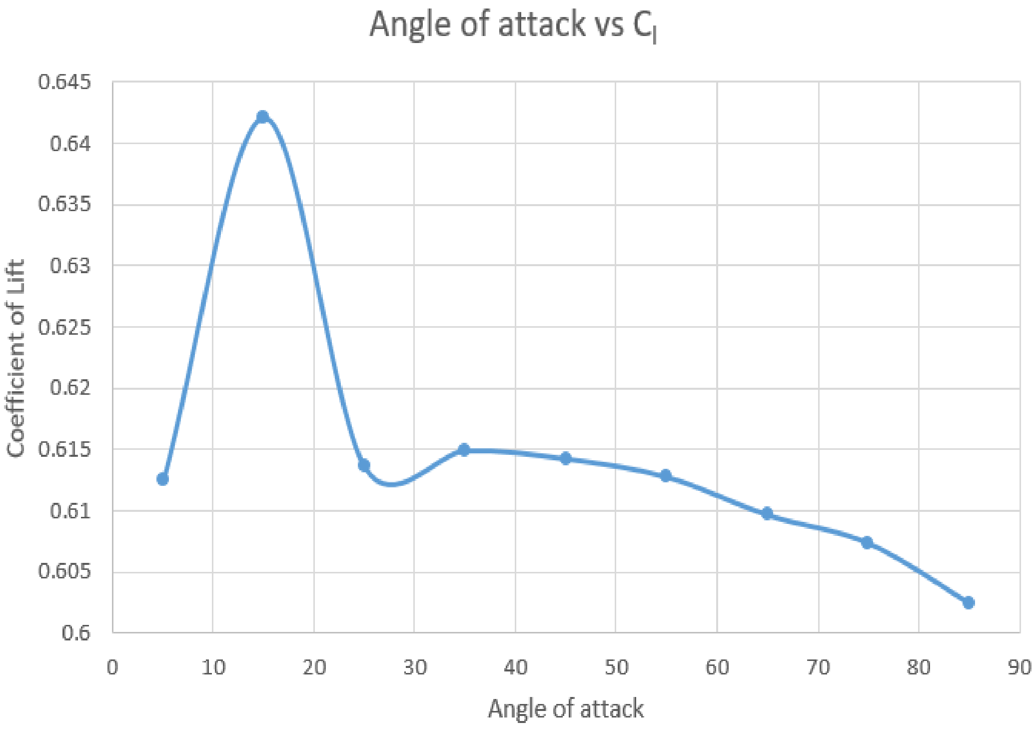

Figure 5.10 Graph between Angle of attack vs C_l for Re= 250000

Table 5.3 C_D and C_L at various angle of attack at Re=250000

S. No	Angle of attack	C_d	C_l	C_l/C_d
1	5	0.0566	0.6343	11.20
2	15	0.0567	0.6348	11.19
3	25	0.0554	0.6204	11.19
4	35	0.0555	0.6198	11.16
5	45	0.0556	0.6197	11.14
6	55	0.05562	0.6196	11.09
7	65	0.05562	0.6211	11.16
8	75	0.0558	0.6204	11.11
9	85	0.05656	0.6189	10.94

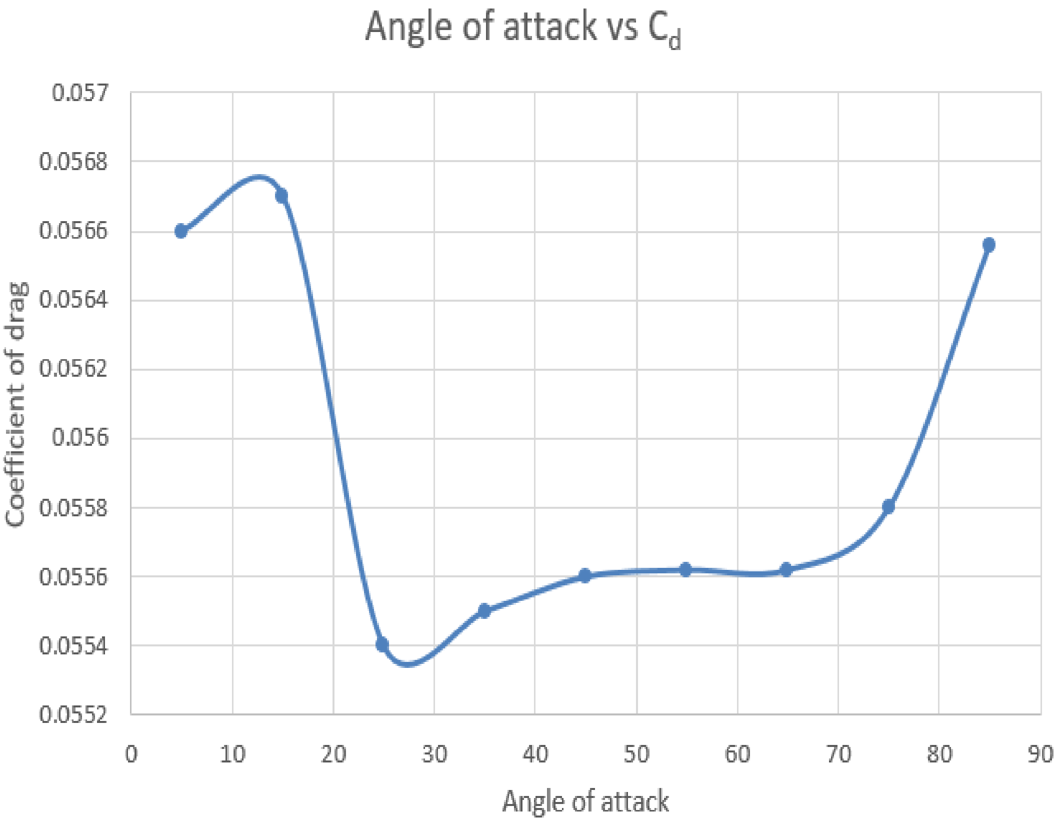

Figure 5.11 Graph between Angle of attack vs C_d for Re= 250000

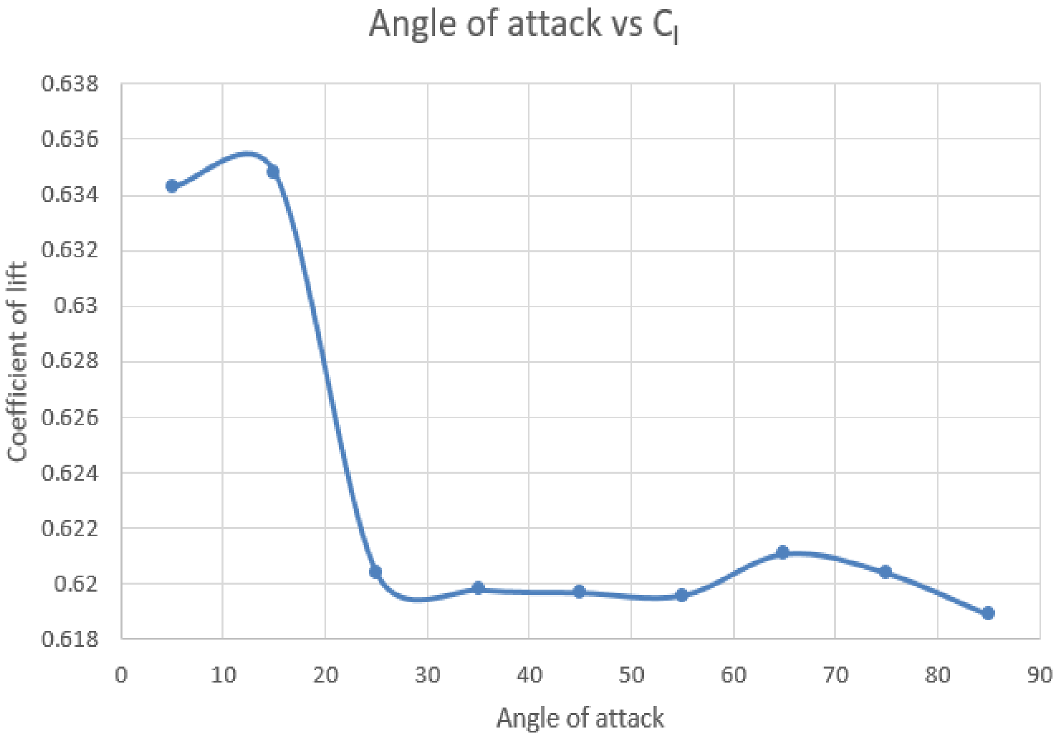

Figure 5.12 Graph between Angle of attack vs C_l for Re= 250000

Table 5.4 C_d and C_l at various angle of attack at Re=500000

S. No.	Angle of attack	C_d	C_l	C_l/ C_d
1	5	0.0559	0.6421	11.48
2	15	0.0556	0.6433	11.48
3	25	0.05574	0.6411	11.50
4	35	0.05556	0.6395	11.51
5	45	0.0555	0.6397	11.63
6	55	0.05556	0.64331	11.48
7	65	0.0562	0.6357	11.31
8	75	0.0558	0.6319	11.32
9	85	0.0546	0.61072	11.18

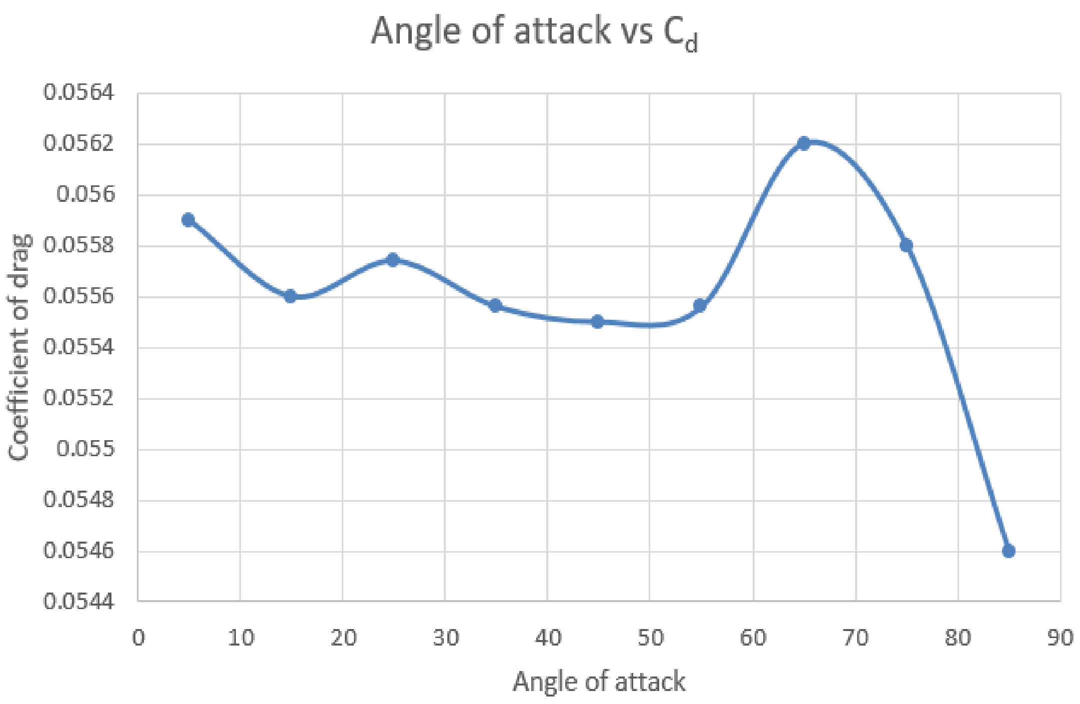

Figure 5.13 Graph between Angle of attack vs C_d for Re= 500000

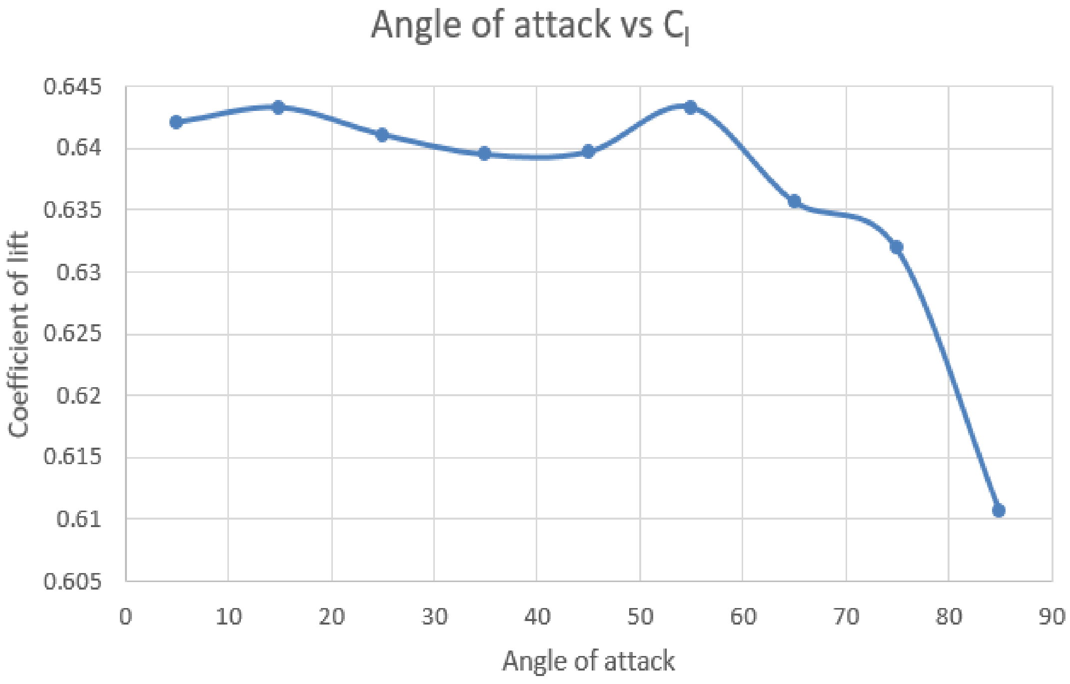

Figure 5.14 Graph between Angle of attack vs C_l for Re= 500000

Table 5.5 Graph between Angle of attack vs C_l for Re= 3000000

S. No	Angle of attack	C_d	C_l	C_l / C_d
1	5	0.0671	0.3357	5.01
2	15	0.07207	0.1629	5.01
3	25	0.0848	0.3188	3.79
4	35	0.0745	0.2148	2.88
5	45	0.0649	0.0519	14.67
6	55	0.0633	0.1296	2.16
7	65	0.04506	0.5303	11.78
8	75	0.0522	0.6524	12.49
9	85	0.0552	0.6523	12.49

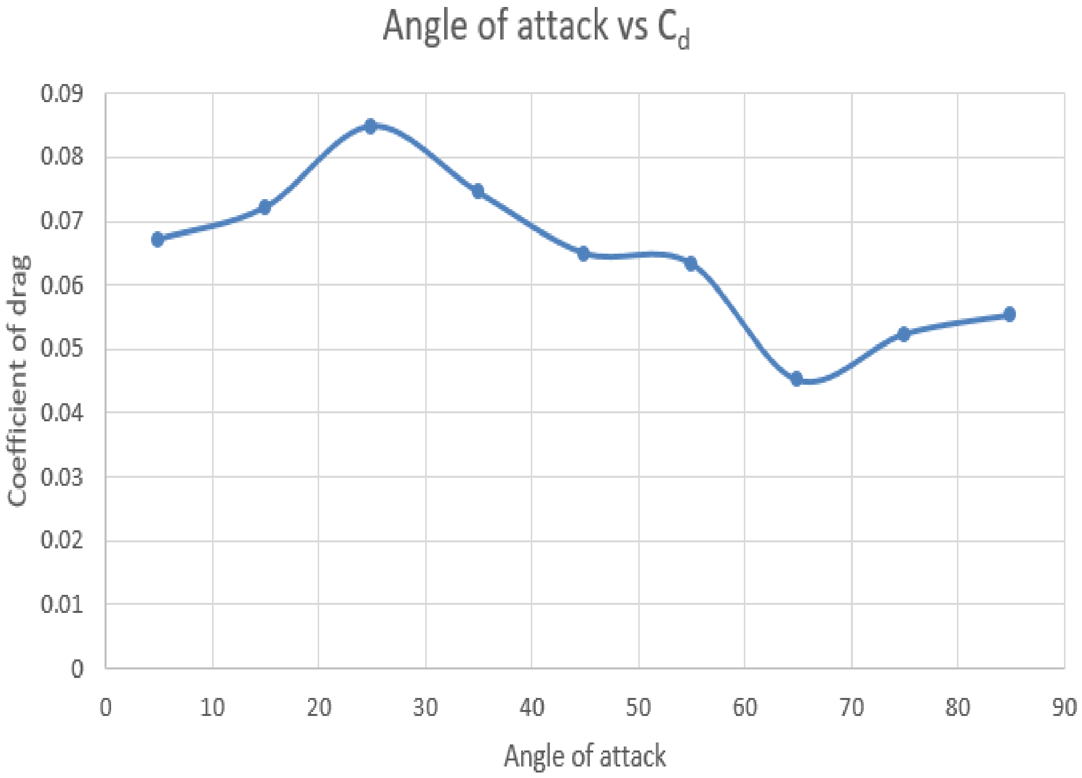

Figure 5.15 Graph between Angle of attack vs C_d for Re= 3000000

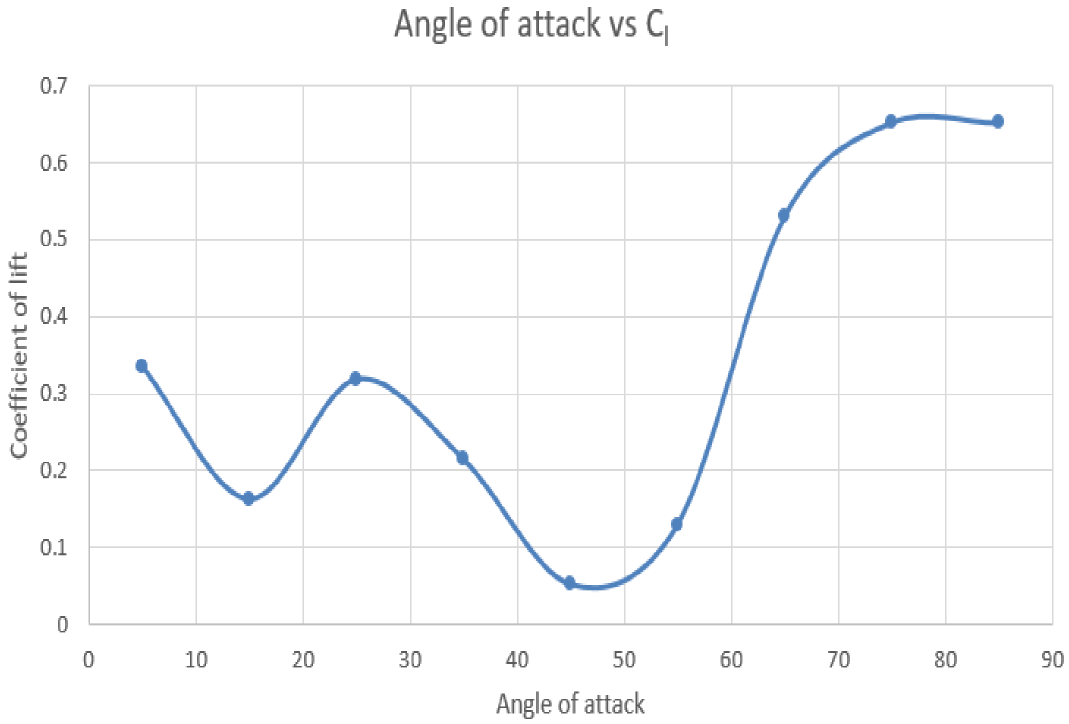

Figure 5.16 Graph between Angle of attack vs C_l for Re= 3000000

Table 5.6 C_D and C_L at various angle of attack at Re=6000000

S. No.	Angle of attack	C_d	C_l	C_l/ C_d
1	5	0.088	0.585	6.647
2	15	0.091	0.8362	9.18
3	25	0.0893	0.9686	10.88
4	35	0.08144	1.0196	12.51
5	45	0.0734	1.0445	14.23
6	55	0.0555	1.0064	18.29
7	65	0.0602	0.2796	4.66
8	75	0.0396	0.5237	13.22
9	85	0.05174	0.6906	13.54

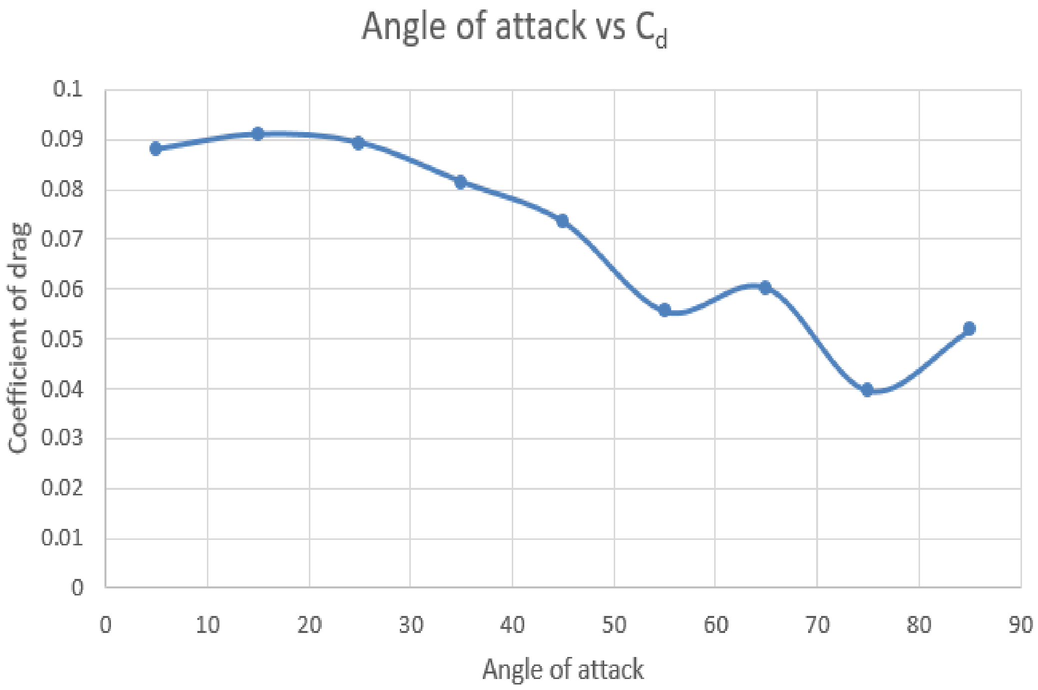

Figure 5.17 Graph between Angle of attack vs C_d for Re= 6000000

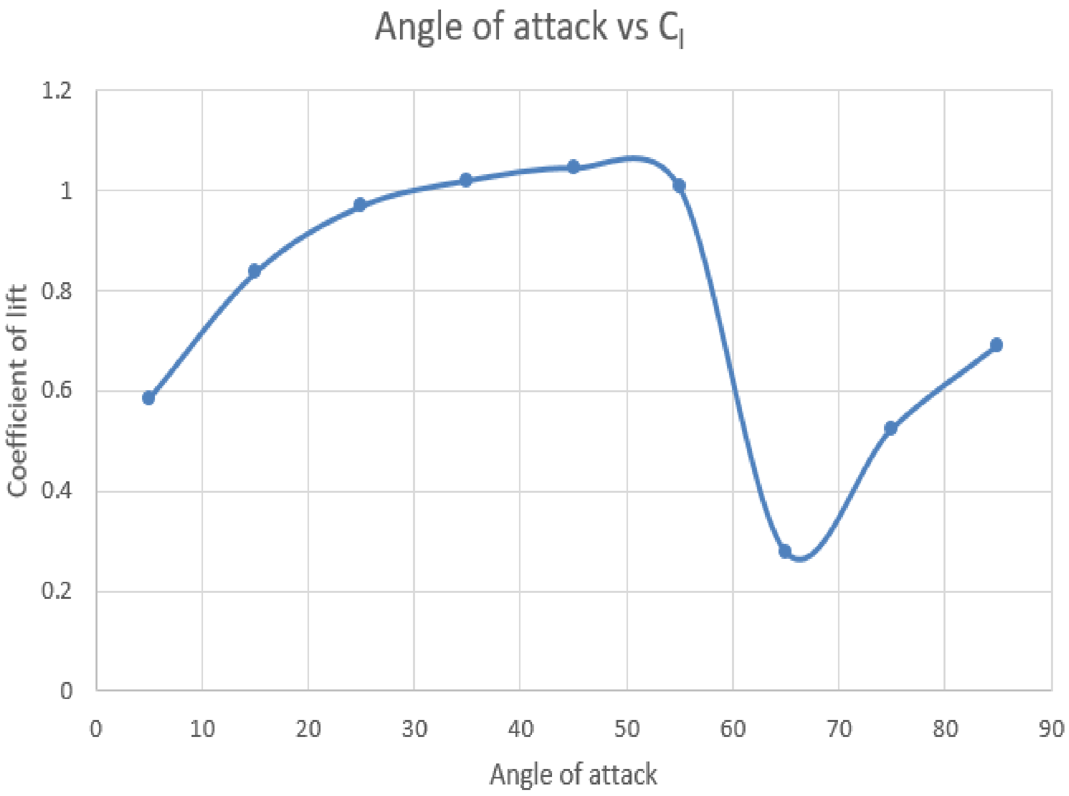

Figure 5.18 Graph between Angle of attack vs C_l for Re= 6000000

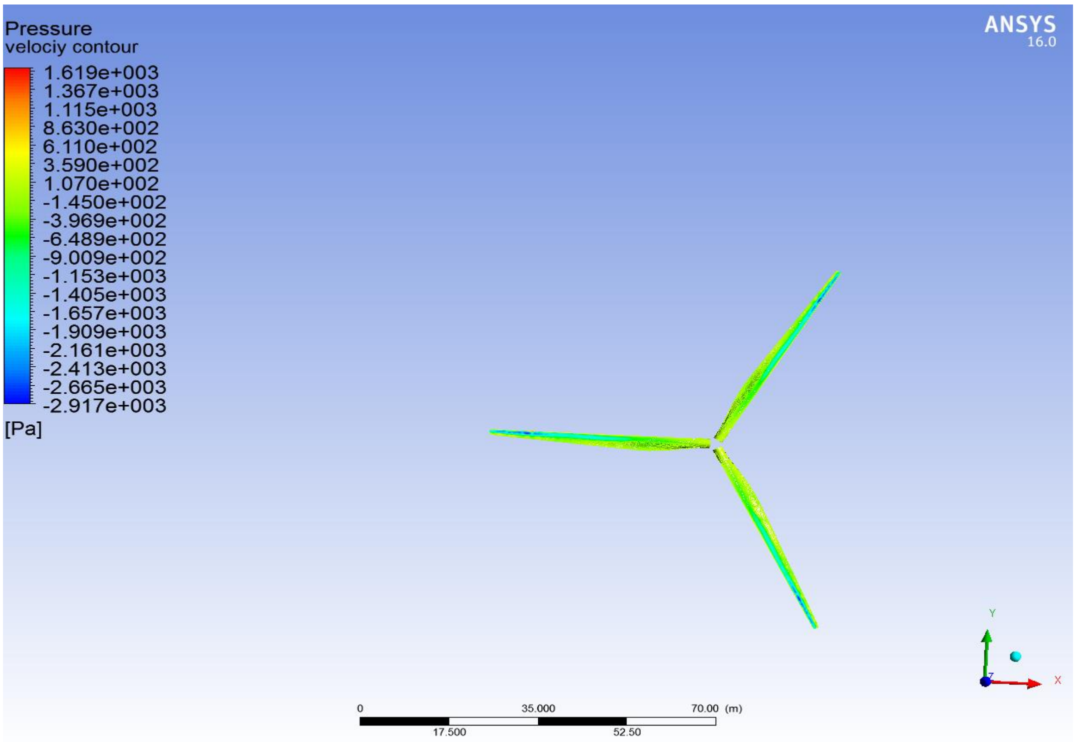

Figure 5.19 Pressure Contour of blade

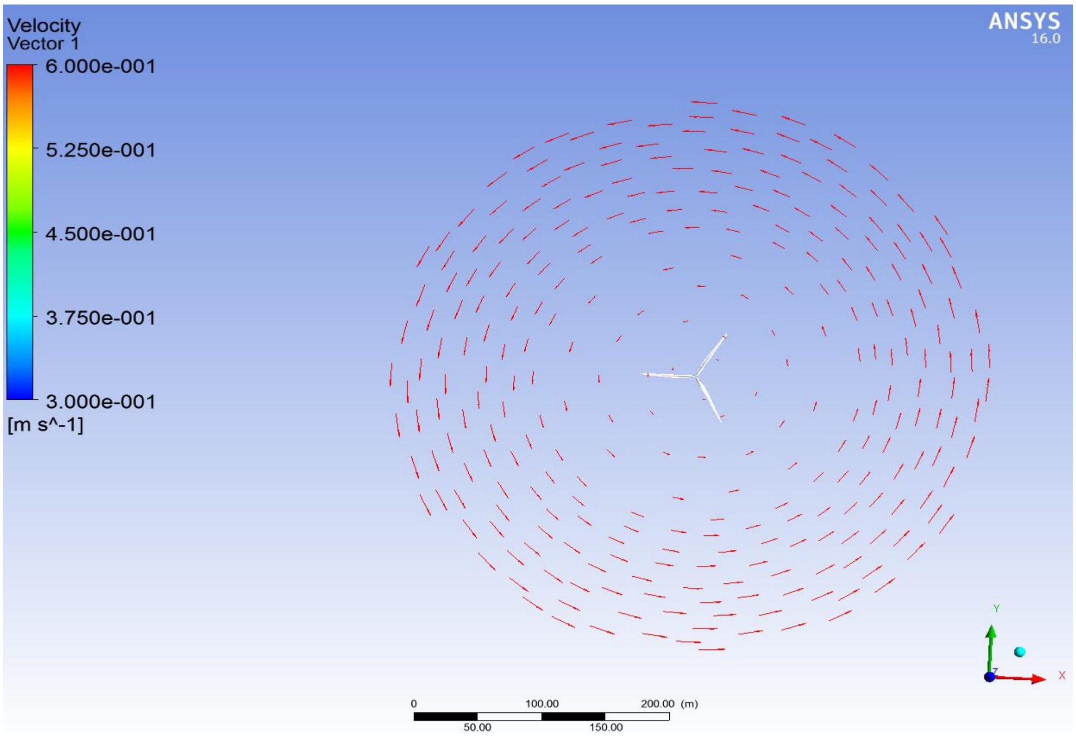

Figure 5.20 Velocity Contour of blade

Figure 5.19 and 5.20 shows the pressure contour and velocity contour over blade finite volume envelope.

CHAPTER 6

CONCLUSION

6.2 Summary

Medim speed rotating wind turbine blade dynamic analysis has been conducted in this work. From the available literature, various forces acting on the blade are accounted and the tapered-twisted aerofoil profile of the blade was generated as a 3D model. By computing element wise cross sectional details from 3D model, a one dimensional finite element beam modelling was considered to discretize the blade from the hub center. Also, a method proposed in literature for the blade dimensions selection was adopted to get the optimum chord and twist angle when the blade tip speed ratio, airfoil type & length of the blade are specified as inputs. The entire work concentrates on the beam finite element modelling of the blade. The modal and transient analysis studies are conducted using 10 beam elements with 6 degrees of freedom per node. Following conclusion is made from this study

- Validation of analysis done [52] for Reynold number 250000, 3000000, and 600000 and for angle of attack between 5^0 , 15^0, and 25^0. It is observe that, close matching in C_l and C_d values are obtained by CFD analysis in comparison to experimental values.
- We found that result of analysis for C_l shows some deviation with experimental results for lower value of angle of attack, however for higher angle of attack close match shows with experimental values.
- In general, we can be conclude that as Reynold number, increases lift forces and drag forces increases. Both CFD and experimental results indicates that, GE’s 1.5xle provides maximum lift and drag at higher Reynold number.

6.1 Future work

As a future work, approximate solution methods for the continuous system of equations have to be applied, so as to validate the result of finite element modelling. Material issues should be introduced to know their effects on dynamic characteristics and failure prediction approaches using polymer composite materials. Testing and analysis of blades can be done on varying climatic conditions such as high humidity, cold regions or high temperature zones. The fatigue, buckling analysis and localized surface roughness on the current blade models determining the structural integrity in real-time approaches, the tower's structural and dynamic interactions must also be taken into account. Fluid structure interaction studies can be done for the flow of wind around the blades and possibilities of formation of eddies and rotor wakes. The area of improving the material characteristics by using layered composites itself is a huge research field for the interested because it offers innumerable combinations of materials to be used to improve effectiveness of the blade.

REFERENCES

[1] Ball, J. (2011). Wind Power Hits a Trough. Wall St. J., Apr 5.

[2] Basu, S., Vinuesa, J. F., & Swift, A. (2008). Dynamic LES modelling of a diurnal cycle. Journal of Applied Meteorology and Climatology, 47(4), 1156-1174.

[3] Bazilevs, Y., Hsu, M. C., Kiendl, J., Wüchner, R., & Bletzinger, K. U. (2011). 3D simulation of wind turbine rotors at full scale. Part II: Fluid–structure interaction modelling with composite blades. *International Journal for Numerical Methods in Fluids*, *65*(1-3), 236-253.

[4] Blackadar, A. K. (1957). Boundary layer wind maxima and their significance for the growth of nocturnal inversions. Bull. Amer. Meteor. Soc, 38(5), 283-290.

[5] Bazilevs, Y., Hsu, M. C., Kiendl, J., Wüchner, R., & Bletzinger, K. U. (2011). 3D simulation of wind turbine rotors at full scale. Part II: Fluid–structure interaction modelling with composite blades. International Journal for Numerical Methods in Fluids, 65(1-3), 236-253.

[7] Brown, R. E. (2000). Rotor wake modelling for flight dynamic simulation of helicopters. AIAA journal, 38(1), 57-63.

[8] Brown, R. E., & Line, A. J. (2005). Efficient high-resolution wake modelling using the vorticity transport equation. AIAA journal, 43(7), 1434.

[9] Calaf, M., Meneveau, C., & Meyers, J. (2010). Large eddy simulation study of fully developed wind-turbine array boundary layers. Physics of fluids, 22(1), 015110.

[10] Christiansen, M. B., & Hasager, C. B. (2006). Using airborne and satellite SAR for wake mapping offshore. Wind Energy, 9(5), 437-455.

[11] Balduzzi, F., Drofelnik, J., Bianchini, A., Ferrara, G., Ferrari, L., & Campobasso, M. S. (2017). Darrieus wind turbine blade unsteady aerodynamics: a three-dimensional Navier-Stokes CFD assessment. Energy, 128, 550-563.

[12] Elliott, D. L., Holladay, C. G., Barchet, W. R., Foote, H. P., & Sandusky, W. F. (1987). Wind energy resource atlas of the United States. NASA STI/Recon Technical Report N, 87.

[13] Fletcher, T. M., & Brown, R. E. (2010). Simulation of wind turbine wake interaction using the vorticity transport model. Wind Energy, 13(7), 587-602.

[14] Frandsen, S., Barthelmie, R., Pryor, S., Rathmann, O., Larsen, S., Hojstrup, J., & Thøgersen, M. (2006). Analytical modelling of wind speed deficit in large offshore wind farms. Wind energy, 9(1-2), 39-53.

[15] Gottschall, J., & Peinke, J. (2007). Stochastic modelling of a wind turbine's power output with special respect to turbulent dynamics. In Journal of Physics: Conference Series (Vol. 75, No. 1, p. 012045). IOP Publishing.

[16] Griffin, D. A. (2002). Blade system design studies volume I: Composite technologies for large wind turbine blades. Sandia National Laboratories, Paper No. SAND-1879.

[18] Hahm, T., & Wubow, S. (2006, February). Turbulent wakes in wind farm configuration. In European Wind Energy conference & exhibition, Athens, Greece (Vol. 27).

[19] Hansen, M. (2008). Aerodynamics of wind turbine 2nd edition.

[20] Davis, C. J. (2012). Computational modelling of wind turbine wake interactions (Doctoral dissertation, Colorado State University).

[21] Jonkman, J. M., & Buhl Jr, M. L. (2005). FAST user's guide. National Renewable Energy Laboratory, Golden, CO, Technical Report No. NREL/EL-500-38230.

[22] Jonkman, J., Butterfield, S., Musial, W., & Scott, G. (2009). Definition of a 5-MW reference wind turbine for offshore system development (No. NREL/TP-500-38060). National Renewable Energy Laboratory (NREL), Golden, CO..

[23] Leishman, G. J. (2006). Principles of helicopter aerodynamics with CD extra. Cambridge university press.

[24] Madsen, H. A., Mikkelsen, R., Øye, S., Bak, C., & Johansen, J. (2007). A Detailed investigation of the Blade Element Momentum (BEM) model based on analytical and numerical results and proposal for modifications of the BEM model. In Journal of Physics: Conference Series (Vol. 75, No. 1, p. 012016). IOP Publishing.

[25] McGowan, J. G., & Connors, S. R. (2000). Windpower: a turn of the century review. Annual Review of Energy and the Environment, 25(1), 147-197.

[26] Menter, F. R. (2009). Review of the shear-stress transport turbulence model experience from an industrial perspective. International Journal of Computational Fluid Dynamics, 23(4), 305-316.

[27] Menter, F. R. (1994). Two-equation eddy-viscosity turbulence models for engineering applications. AIAA journal, 32(8), 1598-1605.

[28] Meyers, J., & Meneveau, C. (2012). Optimal turbine spacing in fully developed wind farm boundary layers. Wind Energy, 15(2), 305-317.

[29] Moriarty, P. J., Holley, W. E., & Butterfield, S. (2002). Effect of turbulence variation on extreme loads prediction for wind turbines. Transactions-American Society of Mechanical Engineers Journal of Solar Energy Engineering, 124(4), 387-395.

[30] Orszag, S. A., Staroselsky, I., Flannery, W. S., & Zhang, Y. (1996). Introduction to renormalization group modelling of turbulence. Simulation and Modelling of Turbulent Flows, 155-184.

[31] O'Sullivan, J. P., Archer, R. A., & Flay, R. G. J. (2011). Consistent boundary conditions for flows within the atmospheric boundary layer. Journal of Wind Engineering and Industrial Aerodynamics, 99(1), 65-77.

[32] Pope, S. B. (2010). Self-conditioned fields for large-eddy simulations of turbulent flows. Journal of Fluid Mechanics, 652, 139-169.

[33] Porté-Agel, F., Wu, Y. T., Lu, H., & Conzemius, R. J. (2011). Large-eddy simulation of atmospheric boundary layer flow through wind turbines and wind farms. Journal of Wind Engineering and Industrial Aerodynamics, 99(4), 154-168.

[34] Saiki, E. M., Moeng, C. H., & Sullivan, P. P. (2000). Large-eddy simulation of the stably stratified planetary boundary layer. Boundary-Layer Meteorology, 95(1), 1-30.

[35] Shih, T. H., Liou, W. W., Shabbir, A., Yang, Z., & Zhu, J. (1995). A new k-ϵ eddy viscosity model for high Reynolds number turbulent flows. Computers & Fluids, 24(3), 227-238.

[36] Sullivan, P. P., & Patton, E. G. (2011). The effect of mesh resolution on convective boundary layer statistics and structures generated by large-eddy simulation. Journal of the Atmospheric Sciences, 68(10), 2395-2415.

[37] Tachos, N. S., Filios, A. E., & Margaris, D. P. (2010). A comparative numerical study of four turbulence models for the prediction of horizontal axis wind turbine flow. Proceedings of the Institution of Mechanical Engineers, Part C: Journal of Mechanical Engineering Science, 224(9), 1973-1979.

[38] Jackson, K. J., Zuteck, M. D., Van Dam, C. P., Standish, K. J., & Berry, D. (2005). Innovative design approaches for large wind turbine blades. Wind Energy, 8(2), 141-171.

[39] Zheng, Y. Q., & ZHAO, R. Z. (2013). Dynamic Response of flexible wind turbine blade. Indonesian Journal of Electrical Engineering and Computer Science, 11(12), 7052-7057.

40] Rule, C. A. N. D. Energy Information Administration, Official Energy Statistics from the US Government. Available on: http://www. Eia. Gov/oiaf/aeo/otheranalysis/aeo2005analysispapers/candr. Html.

[41] Burton, T., Jenkins, N., Sharpe, D., & Bossanyi, E. (2011). Wind energy handbook. John Wiley & Sons.

[42] Manwell, J. F., McGowan, J. G., & Rogers, A. L. (2010). Wind energy explained: theory, design and application. John Wiley & Sons.

[43] Manwell, J. F., McGowan, J. G., & Rogers, A. L. (2010). Wind energy explained: theory, design and application. John Wiley & Sons.

[44] Tande, J. J. (2011). CFD Study of a 10 MW Offshore Horizontal Axis Wind Turbine Blade (Master's thesis, Institutt for fysikk).

[45] White, F. M., & Corfield, I. (2006). Viscous fluid flow (Vol. 3). Boston: McGraw-Hill Higher Education.

[47] Burton, T., Jenkins, N., Sharpe, D., & Bossanyi, E. (2011). Wind energy handbook. John Wiley & Sons.

[48] Research & Innovation European Commission. (2011, April) EU Energy Research[Online]. http://ec.europa.eu/research/energy/eu/research/wind/index_en.htm

[49] ANSYS Inc. (2017, March) Meshing Help. [Online]. http://www1.ansys.com/customer/content/documentation/121/wb_msh.pdf

[50] Wichser, C., & Klink, K. (2008). Low wind speed turbines and wind power potential in Minnesota, USA. Renewable Energy, 33(8), 1749-1758.

[51] Yu, Z., & Tuzuner, A. (2009, July). Fractional 67ehavio wind speed modelling for wind power production estimation. In Power & Energy Society General Meeting, 2009. PES'09. IEEE (pp. 1-7). IEEE.

[52] Abbott, I. H., & Von Doenhoff, A. E. (1959). Theory of wing sections, including a summary of airfoil data. Courier Corporation.

[53] Santhanagopalan, V., Rotea, M. A., & Iungo, G. V. (2017). Performance optimization of a wind turbine column for different incoming wind turbulence. Renewable Energy.

[54] Wang, L., Quant, R., & Kolios, A. (2016). Fluid structure interaction modelling of horizontal-axis wind turbine blades based on CFD and FEA. Journal of Wind Engineering and Industrial Aerodynamics, 158, 11-25.

[55] Li, Q. A., Maeda, T., Kamada, Y., Murata, J., Shimizu, K., Ogasawara, T. & Kasuya, T. (2016). Effect of solidity on aerodynamic forces around straight-bladed vertical axis wind turbine by wind tunnel experiments (depending on number of blades). Renewable Energy, 96, 928-939.

[56] Cai, X., Gu, R., Pan, P., & Zhu, J. (2016). Unsteady aerodynamics simulation of a full-scale horizontal axis wind turbine using CFD methodology. Energy Conversion and Management, 112, 146-156.

[57] Rafiee, R., Tahani, M., & Moradi, M. (2016). Simulation of aeroelastic 68ehaviour in a composite wind turbine blade. Journal of Wind Engineering and Industrial Aerodynamics, 151, 60-69.

[58] Aranake, A. C., Lakshminarayan, V. K., & Duraisamy, K. (2015). Computational analysis of shrouded wind turbine configurations using a 3-dimensional RANS solver. Renewable Energy, 75, 818-832.

[59] Shen, X., Chen, J. G., Zhu, X. C., Liu, P. Y., & Du, Z. H. (2015). Multi-objective optimization of wind turbine blades using lifting surface method. Energy, 90, 1111-1121.

[60] Siddiqui, M. S., Rasheed, A., Kvamsdal, T., & Tabib, M. (2015). Effect of Turbulence Intensity on the Performance of an Offshore Vertical Axis Wind Turbine. Energy Procedia, 80, 312-320.

[61] Micallef, D., & Sant, T. (2015). Loading effects on floating offshore horizontal axis wind turbines in surge motion. Renewable Energy, 83, 737-748.

[62] Montavon, C. (1998). Validation of a non-hydrostatic numerical model to simulate stratified wind fields over complex topography. Journal of wind engineering and industrial aerodynamics, 74, 273-282.

[63] Jones, W. P., & Launder, B. (1972). The prediction of laminarization with a two-equation model of turbulence. International journal of heat and mass transfer, 15(2), 301-314.

[64] WILCOX, D. (1988). Multiscale model for turbulent flows. AIAA journal, 26(11), 1311-1320.